

2019-04-25

Hydrodynamic performance of a pile-supported OWC breakwater: An analytical study

He, F

<http://hdl.handle.net/10026.1/13739>

10.1016/j.apor.2019.03.022

Applied Ocean Research

Elsevier

All content in PEARL is protected by copyright law. Author manuscripts are made available in accordance with publisher policies. Please cite only the published version using the details provided on the item record or document. In the absence of an open licence (e.g. Creative Commons), permissions for further reuse of content should be sought from the publisher or author.

Title:

Hydrodynamic performance of a pile-supported OWC breakwater: an analytical study

Author names and affiliations:

Fang He¹, Huashan Zhang¹, Jiajun Zhao¹, Siming Zheng^{2*} and Gregorio Iglesias^{3,2}

¹Ocean College, Zhejiang University, Zhoushan, Zhejiang 316021, China

²School of Engineering, University of Plymouth, Drake Circus, Plymouth, PL4 8AA, UK

³ MaREI, Environmental Research Institute & School of Engineering, University College Cork, Ireland

***Corresponding author.** E-mail address: siming.zheng@plymouth.ac.uk

Received 23 January 2019,

Revised 15 March 2019,

Accepted 23 March 2019,

Available online 25 April 2019.

<https://doi.org/10.1016/j.apor.2019.03.022>

Hydrodynamic performance of a pile-supported OWC breakwater: an analytical study

Abstract

A pile-supported OWC breakwater is a novel marine structure in which an oscillating water column (OWC) is integrated into a pile-supported breakwater, with a dual function: generating carbon-free energy and providing shelter for port activities by limiting wave transmission. In this work we investigate the hydrodynamics of this novel structure by means of an analytical model based on linear wave theory and matched eigenfunction expansion method. A local increase in the back-wall draft is adopted as an effective strategy to enhance wave power extraction and reduce wave transmission. The effects of chamber breadth, wall draft and air chamber volume on the hydrodynamic performance are examined in detail. We find that optimizing power take-off (PTO) damping for maximum power leads to both satisfactory power extraction and wave transmission, whereas optimizing for minimum wave transmission penalizes power extraction excessively; the former is, therefore, preferable. An appropriate large enough air chamber volume can enhance the bandwidth of high extraction efficiency through the air compressibility effect, with minimum repercussions for wave transmission. Meanwhile, the air chamber volume is found to be not large enough for the air compressibility effect to be relevant at engineering scales. Finally, a two-level practical optimization strategy on PTO damping is adopted. We prove that this strategy yields similar wave power extraction and wave transmission as the ideal optimization approach.

Keywords: oscillating water column; wave energy converter; wave transmission; wave power; air compressibility; optimization

1. Introduction

Conventional breakwaters, whether vertical (caisson), rubble-mound or composite, have the function of providing shelter against waves for port operations. However, with the growing marine economy, marine development and utilization gradually progress into deeper water, and there is increasing concern about the environmental effects of conventional breakwaters, particularly on coastal processes [1, 2]. By contrast, pile-supported breakwaters have less environmental impact, for they permit water and sediment exchange between their seaside and leeside [3]. As wave energy is concentrated near the water surface in deeper waters, pile-supported structures can provide shelter at a cost that is far less sensitive to water depth than that of conventional breakwaters [4]. For these reasons, pile-supported breakwaters have recently emerged as an interesting alternative to traditional breakwaters in deeper waters.

At the same time, ocean waves are one of the most important marine renewable energy resources. The worldwide wave resource is substantial and widely distributed [5]. Wave energy converters (WECs) extract energy from the wave field, and thus reduce the wave height [6, 7]; under certain circumstances, they can play a similar role in breakwaters. The "Mighty Whale" WEC produces a relatively calm sea behind during the open sea tests [8]. At present, the cost of stand-alone in deeper waters remains high, which hampers the development of wave energy [9, 10]. For these reasons, the integration of WECs into breakwaters has been the object of increasing research. An example is OBREC, an overtopping WEC integrated into a rubble-mound breakwater [11, 12]. The integration of oscillating water column (OWC) into vertical (caisson) breakwaters has also been investigated [13]. With respect to pile-supported breakwaters, the subject of this work, the integration of WECs can be beneficial for three main reasons [14-16]. First, pile-supported breakwaters can provide the substructure for the WECs and thus enhance their economic viability. Second, the WECs, by absorbing wave energy, contribute to reducing wave transmission past the breakwaters, and thus improve their efficiency. Finally, the WECs provide electricity to the activities protected by the pile-supported breakwaters, which are usually of certain distances from the mainland [17].

Nowadays, there has emerged a diversity of wave energy converters [18-22]. Compared with other converters, OWC type converter is notably [23-27]. An OWC converter has a pneumatic chamber with a large underwater opening. Incident waves excite the water column inside the chamber, causing it to oscillate; this oscillation forces the air inside the pneumatic chamber to drive a power take-off (PTO) system. Owing to the advantages of simple configuration, fewer moving mechanical parts, good durability and high reliability, OWC converters are particularly suitable for integration with breakwaters [16, 28-30]. Breakwater-mounted OWCs have attracted both the academic and engineering communities. The initial focus of OWC-breakwater integration was bottom-seated, caisson structures, since the work of Ojima [31] in the 1980s; then, the prototypes appeared in different regions, e.g., Sakata, Japan [32], Vizhinjam, India [33], Mutriku, Spain [34], Civitavecchia, Italy [35, 36] and GWK, Germany [37, 38]. At present, OWC-type breakwaters are considered both as bottom-seated, caisson structures and pile-supported structures for deeper water [39]. In the latter, the reduction of wave transmission becomes a key element of the structure's performance, but further study is required. He and Huang [14] investigated the hydrodynamic performance of a pile-supported OWC breakwater through wave-flume experiments, and compared it with more than ten types of innovative pile-supported breakwaters proposed in the literature. They demonstrated that the wave transmission performance was not inferior to other types. Notwithstanding, there is still much room for improvement, not least in

relation to optimization - a fundamental objective for OWC systems [13] which has not been accomplished so far for pile-supported OWC breakwaters.

For stand-alone OWC converters, there have been extensive theoretical studies. The analytical method based on potential theory is well established and could help to understand the fundamental hydrodynamic performance of OWCs. Evans [40] assumed that the water column inside a narrow pneumatic chamber moved like a rigid piston, and focused on how to determine the added mass and radiation damping of the water column. Subsequently, Evans [41] generalized the previous theory and took into account the spatial variation of the water column surface. A reciprocal relationship between the air pressure inside the pneumatic chamber and the diffraction-induced vertical flux was also derived. Sarmento and Falcão [42] considered the compressibility effects of the air inside the pneumatic chamber, and neglected wave diffraction by the immersed OWC. Given that the energy in a sea state is distributed across a range of frequencies, the fundamental objective of the theoretical studies of stand-alone OWCs is to achieve a high extraction efficiency over a broad bandwidth around the peak of the incoming wave spectrum.

As for theoretical studies of OWCs integrated into breakwaters, Martin-Rivas and Mei [43] considered a cylindrical OWC standing at the tip of a thin breakwater and found that, with an appropriate volume of the pneumatic chamber, air compressibility could help broaden the bandwidth of high extraction efficiency. But for pile-supported OWC breakwaters, the effects of air compressibility on wave transmission have not been addressed yet. Sarmento [44] reported wave transmission data for a pile-supported OWC structure, but the immersion adopted was too small to make it function as a breakwater. In the small-scale laboratory tests carried out by He and Huang [14], air compressibility was negligible, and therefore its effects were not considered. One aim of the present analytical study is to explore whether air compressibility may help in reducing wave transmission over a broad bandwidth of frequencies.

The optimal power extraction of the OWC is essentially achieved by the impedance matching between the radiation damping and the PTO characteristic. Since the geometry cannot be easily adjusted once the OWCs have been constructed, most of the previous theoretical studies assumed the PTO characteristic to be ideally controlled for optimization over a broad bandwidth of frequencies [45]; in practice, however, this ideal control is hard to implement. Lovas et al. [46] proposed a more practical control strategy, whereby the PTO characteristic took on only specific values, one for each frequency interval, and found that this approach can be almost as efficient as the ideal control strategy. Another aim of the present analytical study is to explore whether this practical control strategy is also effective in regard to wave transmission over a wide range of frequencies.

The main objective of the present study is to improve the performance of a pile-supported OWC breakwater by increasing power extraction and reducing wave transmission over a broader bandwidth of frequencies. To this end, the hydrodynamic performance of a pile-supported OWC breakwater is analytically investigated. A linear Wells turbine is considered for the PTO, and the compressibility of the air inside the OWC chamber is taken into account. Based on linear potential theory and the method of separation of variables, the spatial potential at any point in the water domain is expressed as a series of Fourier functions. The Galerkin approximation method is adopted to deal with the strong singularities at the sharp edges of the pile-supported OWC breakwater. As indicated by Sarmento [44], the maximum extraction efficiency is only 0.5 for the pile-supported OWC converter with identical front and back walls. In the present study a local increase in the back-wall draft is adopted to improve the performance in an economical way [47]. The effects of chamber breadth and wall draft on the power extraction and wave transmission are examined. Moreover, the air compressibility and practical control strategy are considered in detail.

2. Formulation

2.1 Problem description

Fig.1 shows the two-dimensional pile-supported OWC breakwater in the water of finite depth under consideration in this study. The problem is formulated in a Cartesian coordinate (Oxz) system with x -axis being horizontally rightwards and z -axis being vertically upwards. The origin of the coordinate system O is on the still water level. A train of monochromatic incident waves of small amplitude A and wave frequency ω propagates from $x = -\infty$. The breadth of the pneumatic chamber is denoted by a , and the drafts by d_1 and d_2 for the front and back walls, respectively. The water depth, h , is constant in this study, thus the horizontal sea bed is at $z = -h$. The positions of the front and back walls on the x -axis are $x = x_1$ and $x = x_2$, respectively.

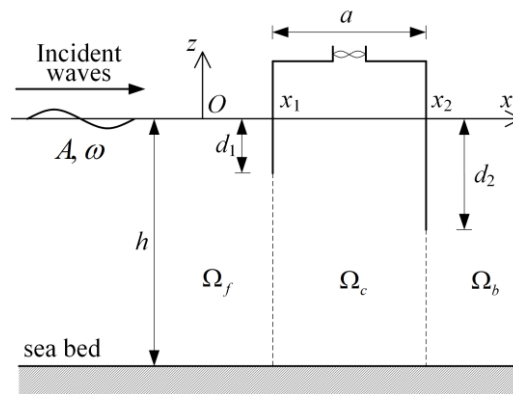


Fig. 1. Problem definition sketch.

2.2 Governing equation and boundary conditions

The fluid is assumed as incompressible, inviscid and irrotational, and the entire fluid field might be described by a velocity potential $\varphi(x, z, t)$ in the frequency domain, where $\varphi(x, z, t)$ is simply harmonic with angular frequency ω and can be written as

$$\varphi(x, z, t) = \text{Re}[\Phi(x, z)e^{-i\omega t}], \quad (1)$$

in which $i = \sqrt{-1}$ and Φ is a complex spatial velocity potential independent of the time t . Φ satisfies the Laplace equation as

$$\frac{\partial^2 \Phi}{\partial x^2} + \frac{\partial^2 \Phi}{\partial z^2} = 0. \quad (2)$$

The spatial velocity potential Φ can be written as a superposition of an incident wave potential $\Phi^{(0)}$, a diffracted wave potential $\Phi^{(1)}$ and a radiated wave potential $\Phi^{(2)}$ as

$$\Phi = \Phi^{(0)} + \Phi^{(1)} + p\Phi^{(2)}, \quad (3)$$

where p is the complex amplitude of the air pressure fluctuation inside the chamber, $\Phi^{(0)}$ describes the nature of incident waves, $\Phi^{(1)}$ describes the response to incident waves due to the structure in the absence of p , and $\Phi^{(2)}$ describes the unit-amplitude response to p in the absence of incident waves. This is a linear superposition, and all the spatial potentials, $\Phi^{(0)}$, $\Phi^{(1)}$ and $\Phi^{(2)}$, satisfy the Laplace equation. For a train of monochromatic incident waves propagating in the x -direction (Fig. 1), the incident wave potential can be written as

$$\Phi^{(0)} = -\frac{igA}{\omega} \frac{\cosh[k(z+h)]}{\cosh(kh)} e^{ikx}, \quad (4)$$

where g is the gravity acceleration, and k is the wave number satisfying the dispersion relation $\omega^2 = gk \tanh(kh)$.

The governing equation and boundary conditions for the diffracted and radiated wave potentials can be written as

$$\frac{\partial^2 \Phi^{(n)}}{\partial x^2} + \frac{\partial^2 \Phi^{(n)}}{\partial z^2} = 0, \quad (5)$$

$$\frac{\partial \Phi^{(n)}}{\partial z} - \frac{\omega^2}{g} \Phi^{(n)} = 0 \quad (z=0, x < x_1 \text{ and } x > x_2), \quad (6)$$

$$\frac{\partial \Phi^{(n)}}{\partial z} - \frac{\omega^2}{g} \Phi^{(n)} = \frac{i\omega\delta_{2,n}}{\rho g} \quad (z=0, x_1 < x < x_2), \quad (7)$$

$$\frac{\partial \Phi^{(n)}}{\partial z} = 0 \quad (z = -h), \quad (8)$$

$$\frac{\partial \Phi^{(n)}}{\partial x} = -\frac{\delta_{1,n} \partial \Phi^{(0)}}{\partial x} \quad (-d_1 < z < 0, x = x_1 \text{ and } -d_2 < z < 0, x = x_2), \quad (9)$$

$$\Phi^{(n)} \text{ outgoing; finite value, } |x| \rightarrow \infty, \quad (10)$$

where the superscripts $n=1$ and 2 denote diffracted and radiated wave potentials, respectively, and $\delta_{i,j}$ is the Kronecker delta,

$$\delta_{i,j} = \begin{cases} 1 & i = j \\ 0 & i \neq j \end{cases}. \quad (11)$$

2.3 Solutions to wave diffraction and radiation

From Eqs. (5)-(10), it is noted that the governing equations for diffracted and radiated wave potentials are the same except the boundary conditions on the wetted surface of the chamber walls and the water surface inside the chamber. Here, the matched eigenfunction expansion method is applied to solve both the wave diffraction and radiation problems [48]. As shown in Fig. 1, the fluid domain is divided into three subdomains as Ω_f , Ω_c and Ω_b by two vertical dash lines, where the subscripts f , c and b are associated with in front of the chamber, inside and under the chamber, and at the back of the chamber, respectively. The spatial potentials of three subdomains are denoted as $\Phi_f^{(n)}$, $\Phi_c^{(n)}$ and $\Phi_b^{(n)}$, where the superscripts $n=1$ and 2 denote again wave diffraction and radiation.

Applying the method of separation of variables, the diffracted and radiated wave potentials in the three subdomains can be expressed as

$$\Phi_f^{(n)} = \sum_{j=0}^{\infty} A_{f,j}^{(n)} e^{\lambda_j x} Z_j(z) \quad \text{in } \Omega_f, \quad (12)$$

$$\Phi_c^{(n)} = \sum_{j=0}^{\infty} (A_{c,j}^{(n)} e^{\lambda_j x} + B_{c,j}^{(n)} e^{-\lambda_j x}) Z_j(z) - \frac{i\delta_{n,2}}{\rho\omega} \quad \text{in } \Omega_c, \quad (13)$$

$$\Phi_b^{(n)} = \sum_{j=0}^{\infty} A_{b,j}^{(n)} e^{-\lambda_j x} Z_j(z) \quad \text{in } \Omega_b, \quad (14)$$

with the normalized eigenfunctions

$$Z_j(z) = N_j^{-0.5} \cos[\lambda_j(h+z)], \quad (15)$$

where

$$N_j = \frac{1}{2} \left[1 + \frac{\sin(2\lambda_j h)}{2\lambda_j h} \right]. \quad (16)$$

The term j represents the wave modes with $j=0$ being the progressive waves and $j>0$ being the evanescent waves. $A_{f,j}^{(n)}$, $A_{c,j}^{(n)}$, $B_{c,j}^{(n)}$ and $A_{b,j}^{(n)}$ are unknown coefficients to be solved. λ_j is the eigenvalue of the j th wave mode, which is given as [49]

$$\lambda_0 = -ik, \quad j=0, \quad (17)$$

$$\omega^2 = -\lambda_j g \tan(\lambda_j h), \quad j=1, 2, 3, \dots \quad (18)$$

The eigenfunctions in Eq. (15) form a complete set of orthogonal functions over $[-h, 0]$, i.e.,

$$\int_{-h}^0 Z_j(z) Z_l(z) dz = h \delta_{j,l}. \quad (19)$$

As indicated by Falnes and McIver [50], this system can be truncated into a finite number of coefficients and solved with the employment of standard eigenfunction matching methods at the interfaces between adjacent subdomains. Since there exist strong singularities at the sharp edges of the chamber walls, the convergence of the system with increasing the number of the truncated terms was found rather slow and it was generally necessary to extrapolate from a sequence of values [50]. To reduce this problem to the solution of a small number of algebraic equations, we adopted the Galerkin approximation method proposed by Evans and Porter [45] to handle the singularities. The following auxiliary functions are introduced to express the water velocities at the x -values of the chamber walls,

$$U_1^{(n)}(z) = \sum_{q=0}^{\infty} A_{1,q}^{(n)} u_{1,q}(z), \quad (20)$$

and

$$U_2^{(n)}(z) = \sum_{q=0}^{\infty} A_{2,q}^{(n)} u_{2,q}(z), \quad (21)$$

where $A_{1,q}^{(n)}$ and $A_{2,q}^{(n)}$ are unknown coefficients to be determined, while $u_{1,q}$ and $u_{2,q}$ are expressed as

$$u_{1,q}(z) = \frac{2(-1)^q}{\pi \sqrt{(h-d_1)^2 - (z+h)^2}} T_{2q} \left(\frac{z+h}{h-d_1} \right), \quad (22)$$

and

$$u_{2,q}(z) = \frac{2(-1)^q}{\pi \sqrt{(h-d_2)^2 - (z+h)^2}} T_{2q} \left(\frac{z+h}{h-d_2} \right), \quad (23)$$

which gives, with T_{2q} as a Chebyshev polynomial [45],

$$\int_{-h}^{-d_1} u_{1,q}(z) Z_l(z) dz = N_l^{-0.5} J_{2q} \{ \lambda_l (h-d_1) \}, \quad (24)$$

and

$$\int_{-h}^{-d_2} u_{2,q}(z) Z_l(z) dz = N_l^{-0.5} J_{2q} \{ \lambda_l (h - d_2) \}, \quad (25)$$

where J_{2q} is the Bessel function of order $2q$.

The diffracted and radiated wave potentials must satisfy the continuity conditions for both the normal velocity and the pressure at the interfaces between adjacent subdomains:

$$\frac{\partial \Phi_f^{(n)}}{\partial x} = \begin{cases} -\delta_{n,1} \frac{\partial \Phi^{(0)}}{\partial x} & (x = x_1, \quad -d_1 < z < 0) \\ U_1^{(n)} & (x = x_1, \quad -h < z < -d_1) \end{cases}, \quad (26)$$

$$\frac{\partial \Phi_c^{(n)}}{\partial x} = \begin{cases} -\delta_{n,1} \frac{\partial \Phi^{(0)}}{\partial x} & (x = x_1, \quad -d_1 < z < 0) \\ U_1^{(n)} & (x = x_1, \quad -h < z < -d_1) \end{cases}, \quad (27)$$

$$\frac{\partial \Phi_c^{(n)}}{\partial x} = \begin{cases} -\delta_{n,1} \frac{\partial \Phi^{(0)}}{\partial x} & (x = x_2, \quad -d_2 < z < 0) \\ U_2^{(n)} & (x = x_2, \quad -h < z < -d_2) \end{cases}, \quad (28)$$

$$\frac{\partial \Phi_b^{(n)}}{\partial x} = \begin{cases} -\delta_{n,1} \frac{\partial \Phi^{(0)}}{\partial x} & (x = x_2, \quad -d_2 < z < 0) \\ U_2^{(n)} & (x = x_2, \quad -h < z < -d_2) \end{cases}, \quad (29)$$

$$\Phi_f^{(n)} = \Phi_c^{(n)} \quad (x = x_1, \quad -h < z < -d_1), \quad (30)$$

$$\Phi_c^{(n)} = \Phi_b^{(n)} \quad (x = x_2, \quad -h < z < -d_2). \quad (31)$$

After multiplying both sides of Eqs. (26)-(31) by $Z_l(z)$, integrating over $[-h, 0]$ and truncating the infinite series into N_l (number of $Z_l(z)$ functions, $l=0,1,2, \dots, N_l$) and N_q (number of Chebyshev polynomial terms T_{2q} , $q=0,1,2, \dots, N_q$), the unknown coefficients can be obtained by solving the linear complex matrix equations.

2.4 Volume flux inside pneumatic chamber

The excitation volume flux can be obtained through an integration of the vertical water velocity, induced by the joint action of incident and diffracted wave potentials, across the free surface inside the chamber as

$$\begin{aligned}
Q_e &= \int_{x_1}^{x_2} \frac{\partial (\Phi^{(0)} + \Phi_c^{(1)})}{\partial z} \Big|_{z=0} dx = \frac{\omega^2}{g} \int_{x_1}^{x_2} (\Phi^{(0)} + \Phi_c^{(1)}) \Big|_{z=0} dx \\
&= -\frac{\omega A}{k} (e^{ikx_2} - e^{ikx_1}) + \frac{\omega^2}{g} \sum_{j=0}^{\infty} \frac{[A_{c,j}^{(1)} (e^{\lambda_j x_2} - e^{\lambda_j x_1}) - B_{c,j}^{(1)} (e^{-\lambda_j x_2} - e^{-\lambda_j x_1})] Z_j(0)}{\lambda_j} .
\end{aligned} \tag{32}$$

Correspondingly, the radiation volume flux can be obtained through an integration of the vertical water velocity, induced by the radiated wave potential $\Phi^{(2)}$, across the free surface inside the chamber as

$$\begin{aligned}
Q_R &= \int_{x_1}^{x_2} \frac{\partial \Phi_c^{(2)}}{\partial z} \Big|_{z=0} dx = \int_{x_1}^{x_2} \left(\frac{\omega^2}{g} \Phi_c^{(2)} \Big|_{z=0} + \frac{i\omega}{\rho g} \right) dx \\
&= \frac{\omega^2}{g} \sum_{j=0}^{\infty} \frac{[A_{c,j}^{(2)} (e^{\lambda_j x_2} - e^{\lambda_j x_1}) - B_{c,j}^{(2)} (e^{-\lambda_j x_2} - e^{-\lambda_j x_1})] Z_j(0)}{\lambda_j} = -(c - i\mu) ,
\end{aligned} \tag{33}$$

where $c = -\text{Re}(Q_R)$ and $\mu = \text{Im}(Q_R)$ are the so-called radiation conductance and radiation susceptance in [45].

By using the Haskind relation [49], which can be derived from Green's identity, over a large fluid domain enclosing the OWC chamber, the excitation volume flux can also be evaluated by

$$Q_e = \frac{2i\rho g A k h A_{f,0}^{(2)}}{Z_0(0)} . \tag{34}$$

Based on Green's theorem or the energy conservation law, the radiation conductance can also be written in terms of the far-field coefficients as

$$c = \omega \rho k h (A_{f,0}^{(2)*} A_{f,0}^{(2)} + A_{b,0}^{(2)*} A_{b,0}^{(2)}) . \tag{35}$$

2.5 Wave power extraction

Following Sarmento and Falcão [42] and Lovas et al. [46], there is a relationship between the complex amplitude of the total volume flux and the air pressure:

$$Q_e + p Q_R = (c_{\text{PTO}} - i\mu_{\text{PTO}}) p , \tag{36}$$

with

$$c_{\text{PTO}} = \frac{KD}{N\rho_0} \tag{37}$$

representing the PTO damping, and

$$\mu_{\text{PTO}} = \frac{\omega V_0}{c_a^2 \rho_0} \tag{38}$$

representing the effects of air compressibility, where K is an empirical coefficient describing the turbine, D is the outer diameter of the turbine rotor, N is the rotational speed of turbine blades, ρ_0 is the static air density, V_0 is the initial air volume inside the pneumatic chamber and c_a is the sound velocity in air. Combining Eqs. (33) and (36), the air pressure fluctuation inside the chamber p can be calculated by

$$p = \frac{Q_e}{c_{\text{PTO}} + c - i(\mu + \mu_{\text{PTO}})}. \quad (39)$$

The time-averaged wave power extraction over one wave period can be expressed as

$$\bar{P} = \frac{1}{2} \frac{c_{\text{PTO}} |Q_e|^2}{(c_{\text{PTO}} + c)^2 + (\mu + \mu_{\text{PTO}})^2}. \quad (40)$$

Thus, the wave power extraction efficiency can be calculated by

$$\eta = \frac{2\bar{P}}{\rho g A^2 C_g}, \quad (41)$$

where C_g is the group velocity of the incident wave,

$$C_g = \frac{\omega}{2k} \left[1 + \frac{2kh}{\sinh(2kh)} \right]. \quad (42)$$

There is an optimal PTO damping which maximizes the wave power extraction efficiency η at each wave frequency. This optimal PTO damping, $c_{\text{opt},\eta}$, can be obtained by imposing $\partial\eta/\partial c_{\text{PTO}} = 0$ [43, 46], which yields

$$c_{\text{opt},\eta} = \sqrt{c^2 + (\mu + \mu_{\text{PTO}})^2}. \quad (43)$$

The maximum time-averaged power output attainable at the wave frequency corresponding to $c_{\text{opt},\eta}$ is

$$\bar{P}_{\text{max}} = \frac{1}{4} \frac{|Q_e|^2}{c + \sqrt{c^2 + (\mu + \mu_{\text{PTO}})^2}}, \quad (44)$$

and the maximum power extraction efficiency attainable at the same frequency is

$$\eta_{\text{max}} = \frac{2\bar{P}_{\text{max}}}{\rho g A^2 C_g}. \quad (45)$$

2.6 Wave reflection and transmission

The modes of evanescent waves can be neglected at the water domain far away from the pile-supported OWC breakwater. On the radiation boundaries $x = \pm x_\infty$, the velocity potentials can be written as

$$\Phi(-x_\infty, z) = -\frac{ig}{\omega} \frac{Z_0(z)}{Z_0(0)} \left[A e^{-ikx_\infty} + \frac{i\omega}{g} Z_0(0) (A_{f,0}^{(1)} + pA_{f,0}^{(2)}) e^{ikx_\infty} \right], \quad (46)$$

and

$$\Phi(x_\infty, z) = -\frac{ig}{\omega} \frac{Z_0(z)}{Z_0(0)} \left[A e^{ikx_\infty} + \frac{i\omega}{g} Z_0(0) (A_{b,0}^{(1)} + pA_{b,0}^{(2)}) e^{ikx_\infty} \right]. \quad (47)$$

Consequently, by calculating the wave amplitudes at the radiation boundaries $x = \pm x_\infty$, the wave reflection coefficient R and wave transmission coefficient T can be evaluated as

$$R = \left| \frac{\omega Z_0(0)}{gA} (A_{f,0}^{(1)} + pA_{f,0}^{(2)}) \right|, \quad (48)$$

$$T = \left| 1 + \frac{i\omega Z_0(0)}{gA} (A_{b,0}^{(1)} + pA_{b,0}^{(2)}) \right|. \quad (49)$$

There is an optimal PTO damping, $c_{\text{opt},T}$, which minimizes wave transmission T at each wave frequency, and can be obtained by imposing $\partial T / \partial c_{\text{PTO}} = 0$. As the expression of $c_{\text{opt},T}$ is somewhat cumbersome, it is given in the

Appendix. The minimum wave transmission coefficient corresponding to $c_{\text{opt},T}$ is

$$T_{\min} = \left| 1 + \frac{i\omega Z_0(0)}{gA} \left(A_{b,0}^{(1)} + \frac{Q_e A_{b,0}^{(2)}}{c_{\text{opt},T} + c - i(\mu + \mu_{\text{PTO}})} \right) \right|. \quad (50)$$

3. Results and discussion

The above analytical solution was implemented through a self-programming code. A convergence test was carried out to examine the truncated number N_l of $Z_l(z)$ functions and the truncated number N_q of Chebyshev polynomial terms T_{2q} . It was demonstrated that $N_l=50$ and $N_q=10$ are enough to guarantee sufficiently accurate results for the entire computed range of wave conditions in the present study. In the subsequent computations, the following values are used, unless otherwise specified: density ratio $\rho / \rho_0 = 1000$, sound velocity in air $c_a = 340$ m/s, gravity acceleration $g = 9.81$ m/s², and air chamber volume $V_0 = 0.1ah$.

3.1 Model validation

The present model is firstly validated with the analytical results published by Falnes and McIver [50]. For comparison, the analytical results in this subsection follow the definition of dimensionless variables in Falnes and McIver [50] as

$$\bar{c} = \frac{\rho g c}{\omega a}, \quad \bar{\mu} = \frac{\rho g \mu}{\omega a}, \quad \bar{Q}_e = \frac{|Q_e|}{\omega a A}, \quad \varphi_e = \arg(Q_e). \quad (51)$$

In this case the parameters for the calculation are: $d_1/h=0.15$, $d_2/h=0.25$, $a/h=0.1$ and $V_0=0.1ah$. Fig. 2 compares the dimensionless excitation volume flux, in terms of amplitude and phase, versus the dimensionless wave number kh with the corresponding results in Falnes and McIver [50], while Fig.3 compares the dimensionless radiation conductance and susceptance. In calculations, the reciprocal relation linking the scattering problem to the radiation problem is also checked for validation. The excitation volume flux evaluated based on the Haskind relation in Eq. (34) is presented in Fig.2, while the radiation conductance evaluated in terms of far-field coefficients in Eq. (35) is presented in Fig.3. Both Figs.2 and 3 evidently show that various results obtained by the present model agree excellently with the analytical results published by Falnes and McIver [50]. The present model is well validated.

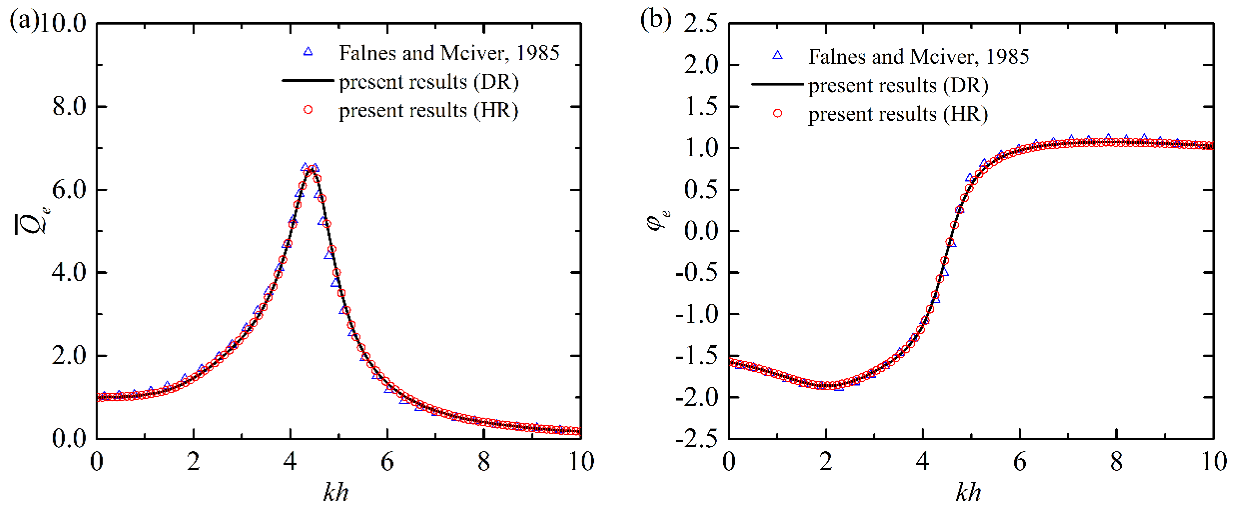


Fig.2 Dimensionless excitation volume flux versus dimensionless wave number kh for $d_1/h=0.15$, $d_2/h=0.25$, $a/h=0.1$ and $V_0=0.1ah$: (a) amplitude and (b) phase. [In the legend, DR and HR indicate that Q_e is calculated directly from Eq. (32) or based on the Haskind relation in Eq. (34), respectively].

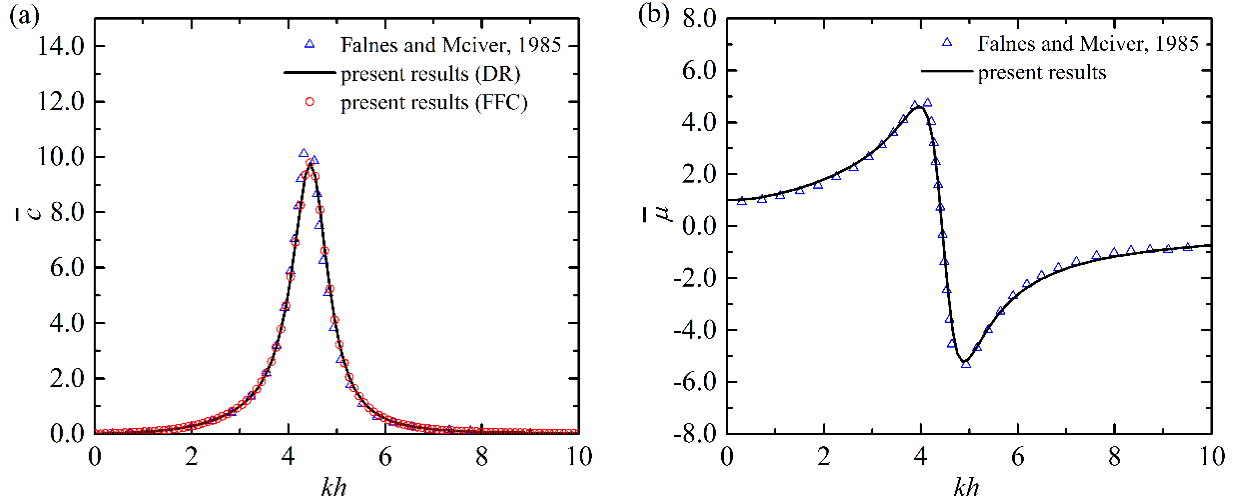


Fig.3 Dimensionless radiation coefficients versus dimensionless wave number kh for $d_1/h=0.15$, $d_2/h=0.25$, $a/h=0.1$ and $V_0=0.1ah$: (a) radiation conductance \bar{c} and (b) radiation susceptance $\bar{\mu}$. [In the legend, DR and FFC indicate that \bar{c} is calculated directly from Eq. (33) or in terms of far-field coefficients in Eq. (35), respectively].

Besides, the conservation of wave energy for the present model is also checked. Fig. 4 shows the variations of wave reflection coefficient R , wave transmission coefficient T , power extraction efficiency η , and a sum of power ratio $R^2 + T^2 + \eta$ versus the dimensionless wave number kh .

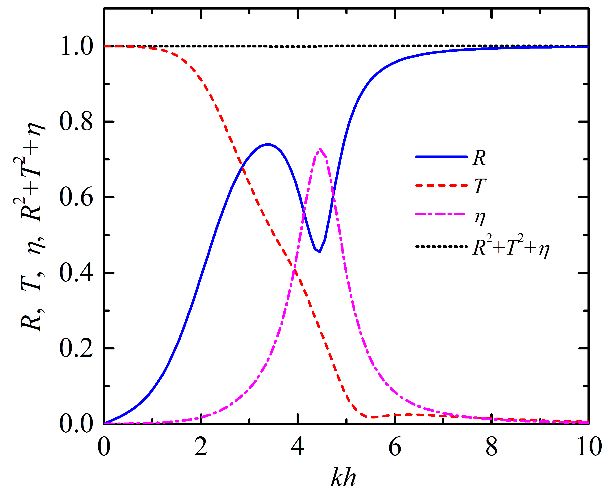


Fig.4 Variations of R , T , η and $R^2 + T^2 + \eta$ versus dimensionless wave number kh for $h=20$ m, $d_1/h=0.15$, $d_2/a=0.25$, $a/h=0.1$, $V_0=0.1ah$ and $c_{PTO}=6.0\sqrt{h/g}/\rho$.

Here the calculating parameters are: $d_1/h = 0.15$, $d_2/h = 0.25$, $a/h = 0.1$, $V_0 = 0.1ah$ and

$c_{PTO} = 6.0\sqrt{h/g}/\rho$. It can be seen that the total power ratio $R^2 + T^2 + \eta$ is always unity, which means that wave energy is conserved, i.e., the present model is conservative. The conservation of wave energy validates the present model from yet another aspect.

In the following, the validated analytical model will be adopted to study the effects of ratio of wall drafts, chamber breadth, wall draft and air chamber volume on the power extraction and wave transmission. From the next subsection, we will follow the non-dimension definition in Lovas et al. [46] as

$$\bar{c}_{PTO} = c_{PTO}\rho\sqrt{g/h}, \quad \bar{\mu}_0 = -\mu_{PTO}\rho\sqrt{g/h} = -\frac{\omega V_0\rho\sqrt{g/h}}{\rho_0 c_a^2}, \quad \bar{c}_{opt,\eta} = c_{opt,\eta}\rho\sqrt{g/h}, \quad \bar{c}_{opt,T} = c_{opt,T}\rho\sqrt{g/h} \quad (52)$$

and the radiation susceptance is correspondingly renormalized as $\bar{\mu} = \mu\rho\sqrt{g/h}$.

Hereinafter, the subscript “opt, η ” represents the corresponding physical quantities; thus, $c_{opt,\eta}$, $T_{opt,\eta}$ and $R_{opt,\eta}$, for instance, correspond to the case in which wave power extraction is optimized as η_{max} . Conversely, the subscript “opt, T ” denotes the corresponding physical quantities, so $c_{opt,T}$, $\eta_{opt,T}$ and $R_{opt,T}$ are obtained when wave transmission is optimized as T_{min} .

3.2 Ratio of wall drafts

Sarmiento [44] indicated that the peak of optimal power extraction efficiency attainable at each wave frequency could reach only 0.5 if the front and back walls of a pile-supported OWC converter are identical. Intuitively, a locally increased back-wall draft could reflect part of wave energy into the OWC chamber and thus contribute to reducing wave transmission past the back wall [47]. In this study, a local increase in the back-wall draft is explored as an effective strategy to improve the performance of a pile-supported OWC breakwater. The effects of the ratio of wall drafts on the wave power extraction and the protection against wave action are examined.

The variations in optimal power extraction efficiency η_{max} and corresponding wave transmission coefficient $T_{opt,\eta}$ versus the ratio of wall drafts d_2/d_1 are shown in Fig. 5. The calculation parameters are: $a/h = 0.1$, $d_1/h = 0.15$ and $V_0 = 0.1ah$. If the d_2/d_1 ratio reaches 20/3, the back wall will penetrate the water depth to the sea bed and the geometry will become a bottom-seated OWC-type caisson breakwater. Here we should mention that the

present analytical model is not suitable for this limiting condition and thus we confine the range of d_2 / d_1 within [1, 5]. As shown in Fig. 5(a), the local increase in the back-wall draft significantly affects the η_{\max} for d_2 / d_1 ranging from 1.0 to a certain value, whereas a further increase in d_2 / d_1 has only little influence. This certain value of d_2 / d_1 differs with wave frequency (kh) and is generally smaller for shorter waves. This is mainly because the exponential decay of fluid velocity with increasing underwater depth is faster for shorter waves. Except for the longest wave ($kh=2$), η_{\max} is mainly affected within the range $1.0 < d_2 / d_1 < 3.0$, implying that a locally increased back-wall draft contributes to enhancing wave power extraction. Taking $kh=4$ as an example, there exists an optimal $d_2 / d_1=2.72$ which makes η_{\max} reach a peak of 0.92; by contrast, η_{\max} is only 0.26 when the front and back walls are identical (i.e., $d_2 / d_1=1$).

The local increase in the back-wall draft may affect the wave transmission in two ways. On the one hand, a deeper back wall could increase the shelter effect; on the other, the new chamber geometry would alter both the resonance frequency and the radiation damping of the water column inside the chamber, so the interference between scattered and radiated waves could be affected. Fig. 5(b) shows that $T_{\text{opt},\eta}$ generally decreases with increasing d_2 / d_1 . To obtain a small value of $T_{\text{opt},\eta}$, a smaller value of d_2 / d_1 is required for the shorter incident waves. Taking $T_{\text{opt},\eta}=0.09$ as an example, $d_2 / d_1=1.0, 1.3, 1.9, 2.2$ and 3.1 is required for $kh=7, 6, 5, 4$, and 3 , respectively, from which it can be inferred that the increased shelter effect dominates. For $kh=5$, there exists a local valley of $T_{\text{opt},\eta}=0.50$ at $d_2 / d_1=1.06$ which is due to the resonance, but its influence on the wave transmission is negligible compared with the shelter effect.

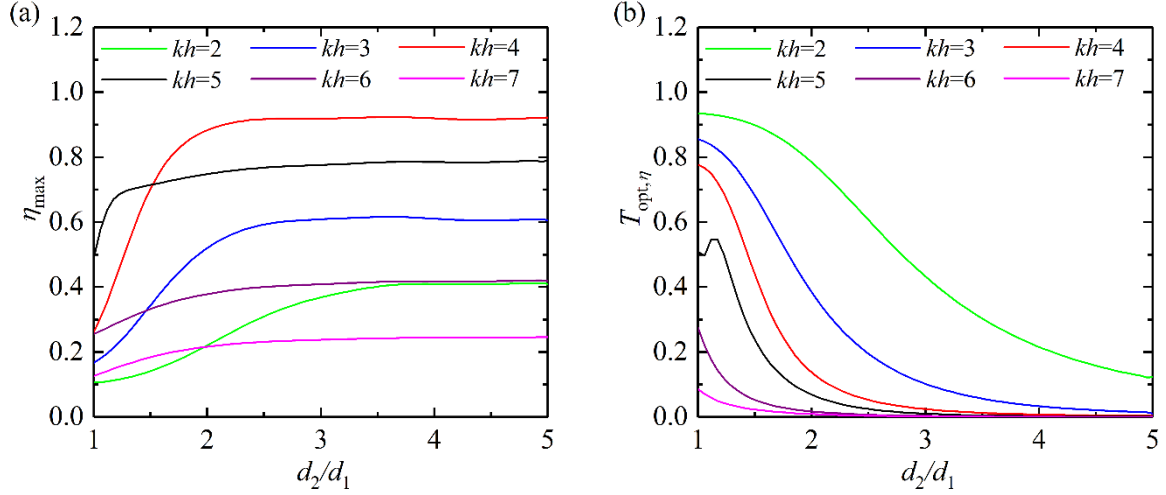


Fig. 5 (a) Optimal power extraction efficiency η_{\max} and (b) the corresponding wave transmission coefficient $T_{\text{opt},\eta}$ versus the ratio of wall drafts d_2/d_1 for different dimensionless wave numbers kh [$h=20$ m, $a/h=0.1$, $d_1/h=0.15$ and $V_0=0.1ah$].

3.3 Chamber breadth and wall draft

The breadth and draft are two important parameters affecting the hydrodynamic performance and the construction costs of a pile-supported breakwater [14]. The effects of chamber breadth and wall draft of pile-supported OWC breakwater on the wave power extraction and the protection against wave action are examined in this subsection. In the previous subsection it was concluded that a local increase in the back-wall draft could increase wave power extraction and decrease wave transmission, yet a too large d_2/d_1 may increase the construction costs. In the subsequent computations, a local increase of $0.1h$ in the back-wall draft, i.e., $d_2 = d_1 + 0.1h$, will be used unless otherwise specified. Two optimization methods, i.e., optimizing the PTO damping as $c_{\text{opt},\eta}$ to maximize wave power extraction efficiency ($\eta = \eta_{\max}$) at each wave frequency, and optimizing the PTO damping as $c_{\text{opt},T}$ to minimize wave transmission ($T = T_{\min}$) at each wave frequency, are adopted. Both the optimal wave power extraction efficiency η_{\max} with the corresponding wave transmission $T_{\text{opt},\eta}$ and the optimal wave transmission T_{\min} with the corresponding wave power extraction $\eta_{\text{opt},T}$ will be considered.

Fig. 6 illustrates the effects of chamber breadth when the PTO damping is optimized for maximizing the wave power extraction efficiency. The calculation parameters are: $h=20$ m, $d_1/h=0.15$, $d_2/h=0.25$, $V_0=0.1ah$, $a/h=0.05, 0.1, 0.15, 0.2$ and 0.3 . The variations of optimal power extraction efficiency η_{\max} , optimal dimensionless PTO damping $\bar{c}_{\text{opt},\eta}$, wave transmission coefficient $T_{\text{opt},\eta}$ and wave reflection coefficient $R_{\text{opt},\eta}$ are shown versus dimensionless wave number kh . We can see from Fig. 6(a) that the peaks of η_{\max} are 0.984, 0.955, 0.923, 0.893 and 0.836 for $a/h=0.05, 0.1, 0.15, 0.2$ and 0.3 , and occur at $kh=5.1, 4.5, 4.1, 3.8$ and 3.4 , respectively. In general, the peak of η_{\max} is a little lower for a wider chamber and occurs at a longer wave. The observation of unequal peaks of η_{\max} for different chamber breadths is different from the bottom-seated OWC device whose peaks of η_{\max} are always 1.0 [45]. This is because that a wider chamber resonates at a longer wave which can more easily pass through the back wall of the pile-supported OWC breakwater and the transmitted wave energy reduces the extracted wave power at resonance. Nevertheless, the peaks of η_{\max} still remain at a high level. In addition, it is noted that the bandwidth of η_{\max} is broader for a wider chamber, which is consistent with the bottom-seated OWC device [45]. Comparing Fig. 6 (b) with Fig. 6(a), the corresponding peaks of $\bar{c}_{\text{opt},\eta}$ occur at roughly the same wave frequencies. The peak of η_{\max} is in principle achieved by two conditions, i.e., the OWC resonates at the natural frequency and meanwhile the PTO damping matches the radiation damping [43]. Fig. 6 (b) indicated that a larger optimal PTO damping is desired for a wider chamber when resonance occurs.

As shown in Fig. 6(c), when the PTO damping is optimized for η_{\max} , the corresponding wave transmission $T_{\text{opt},\eta}$ is not markedly different. Indeed, the largest difference in $T_{\text{opt},\eta}$ for a given kh is only 0.181 between the widest chamber ($a/h=0.3$) and narrowest chamber ($a/h=0.05$), over all wave frequencies tested in this study. The trends of $T_{\text{opt},\eta}$ for all chamber breadths are of approximately monotonic decrease with increasing kh . It is interesting noted that $T_{\text{opt},\eta}$ for each chamber breadth has a local valley at kh slightly smaller than resonance and a local peak at kh slightly larger than resonance. This local impact to the approximately monotonic decreasing $T_{\text{opt},\eta}$ can be seen as relatively weak. Fig. 6(d) shows that with increasing kh , $R_{\text{opt},\eta}$ firstly increases to a turning point, then decreases to a local minimum of nearly zero around kh where resonance occurs, after that $R_{\text{opt},\eta}$

monotonically increases, and finally reaches almost one at the largest kh . A narrower chamber has a higher turning point and generally reflects more wave energy for long waves, e.g., $kh < 3.0$, whereas reflects less for short waves, e.g., $kh > 5.0$.

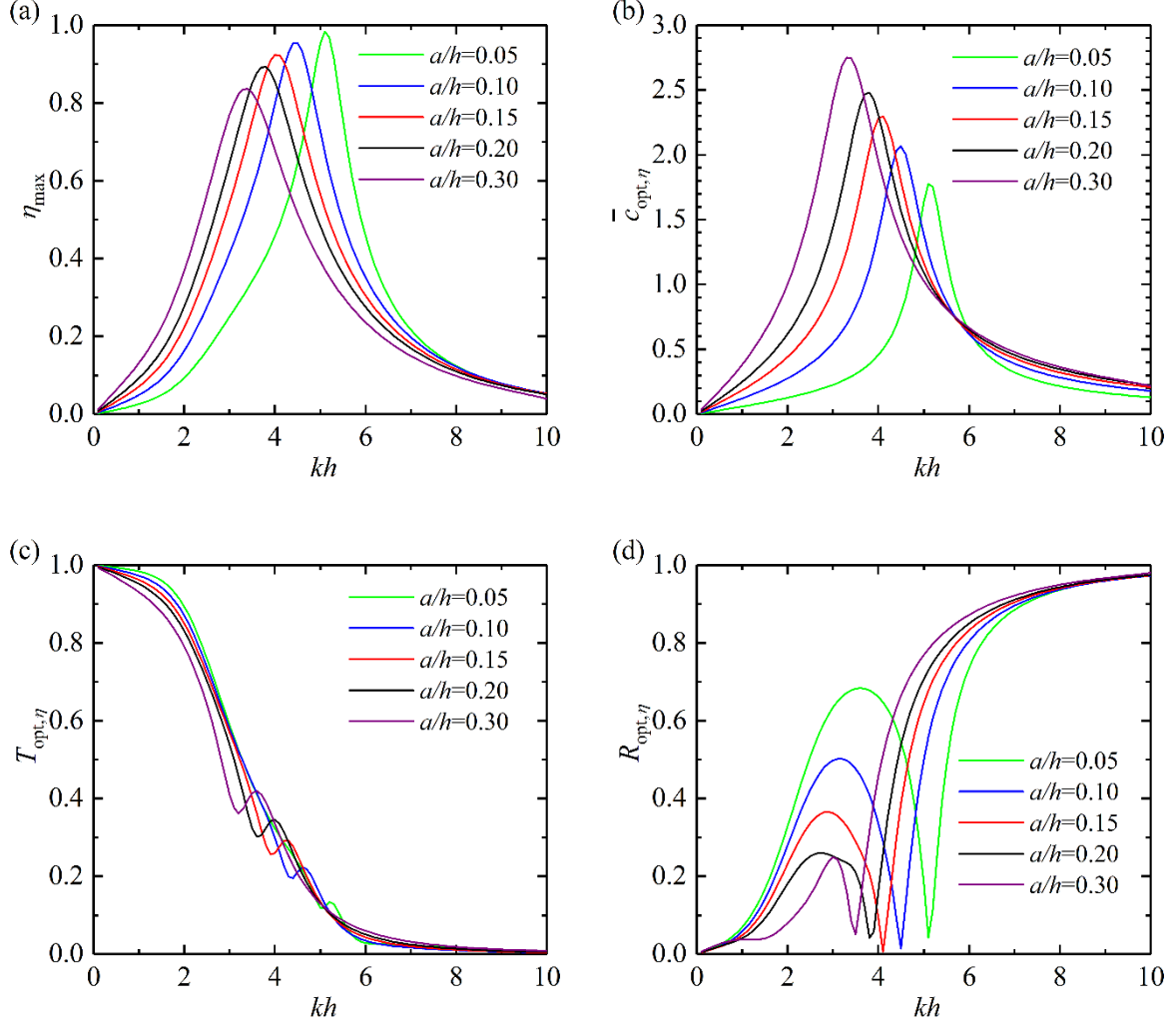


Fig.6 (a) Optimal power extraction efficiency η_{\max} , (b) optimal dimensionless PTO damping $\bar{c}_{\text{opt},\eta}$, (c) wave transmission coefficient $T_{\text{opt},\eta}$ and (d) wave reflection coefficient $R_{\text{opt},\eta}$ versus dimensionless wave number kh for different chamber breadths a/h [$h=20$ m, $d_1/h=0.15$, $d_2/h=0.25$ and $V_0=0.1ah$].

Fig. 7 illustrates the effects of chamber breadth when the PTO damping is optimized in the range of $\bar{c}_{\text{PTO}} \in [0,10]$, i.e., $\bar{c}_{\text{ul}}=10$, for minimizing the wave transmission. The variations of power extraction efficiency $\eta_{\text{opt},T}$, optimal dimensionless PTO damping $\bar{c}_{\text{opt},T}$, optimal wave transmission coefficient T_{\min} and wave reflection coefficient $R_{\text{opt},T}$ are shown versus dimensionless wave number kh . Comparing Fig. 7(a) with Fig. 6(a), the main

difference is that there exists a local sharp valley of $\eta_{opt,T}$ for each chamber, which occurs at longer wave for a wider chamber. This nearly-zero local valley greatly harms the wave power extraction around. We can see from Fig. 7(b) that the $c_{opt,T}$ corresponding to the valley of $\eta_{opt,T}$ is nearly zero. With increasing kh , the $c_{opt,T}$ value of a wider chamber reaches the nearly-zero value and the set upper limit c_{ul} more rapidly, and remains at c_{ul} over a wider range of wave frequencies. This is markedly different from the trends of $c_{opt,\eta}$ that can be observed in Fig. 6(b).

Comparing Fig. 7(c) with Fig. 6(c), there still exist a local valley and a local peak of wave transmission for each chamber breadth. The local valley of T_{min} is much lower than the local valley of $T_{opt,\eta}$ for the same chamber breadth, and the local peaks of T_{min} and $T_{opt,\eta}$ are comparable. From around kh where the local valley occurs, T_{min} is a little lower than $T_{opt,\eta}$ over a certain range of kh , and this range is broader for a wider chamber. In contrast, for kh lower than where the local valley occurs, T_{min} is almost the same as $T_{opt,\eta}$. That is, T_{min} is only smaller than $T_{opt,\eta}$ at the wave frequencies where the wave transmission is already small, whereas at the wave frequencies with large wave transmission, T_{min} and $T_{opt,\eta}$ are almost the same. Compared with optimizing the PTO damping as $c_{opt,\eta}$ for η_{max} , optimizing the PTO damping as $c_{opt,T}$ for T_{min} hardly improves the performance in terms of providing wave shelter, but does hamper the performance in terms of wave power extraction. Taking $a/h = 0.10$ as an example, the local valley of T_{min} is nearly zero at $kh = 4.3$. The corresponding $\eta_{opt,T}$ at $kh = 4.3$ in Fig. 7(a) and $c_{opt,T}$ at $kh = 4.3$ in Fig. 7(b) are also nearly zero, whereas the corresponding $R_{opt,T}$ at $kh = 4.3$ in Fig. 7(d) is nearly one, implying that the turbine practically stops and almost all the wave energy is reflected. Comparing Fig. 7(d) with Fig. 6(d), it is clear that $c_{opt,T}$ makes the pile-supported OWC breakwater function more as a reflective structure than as an absorbing system, thereby violating its original multifunction conception.

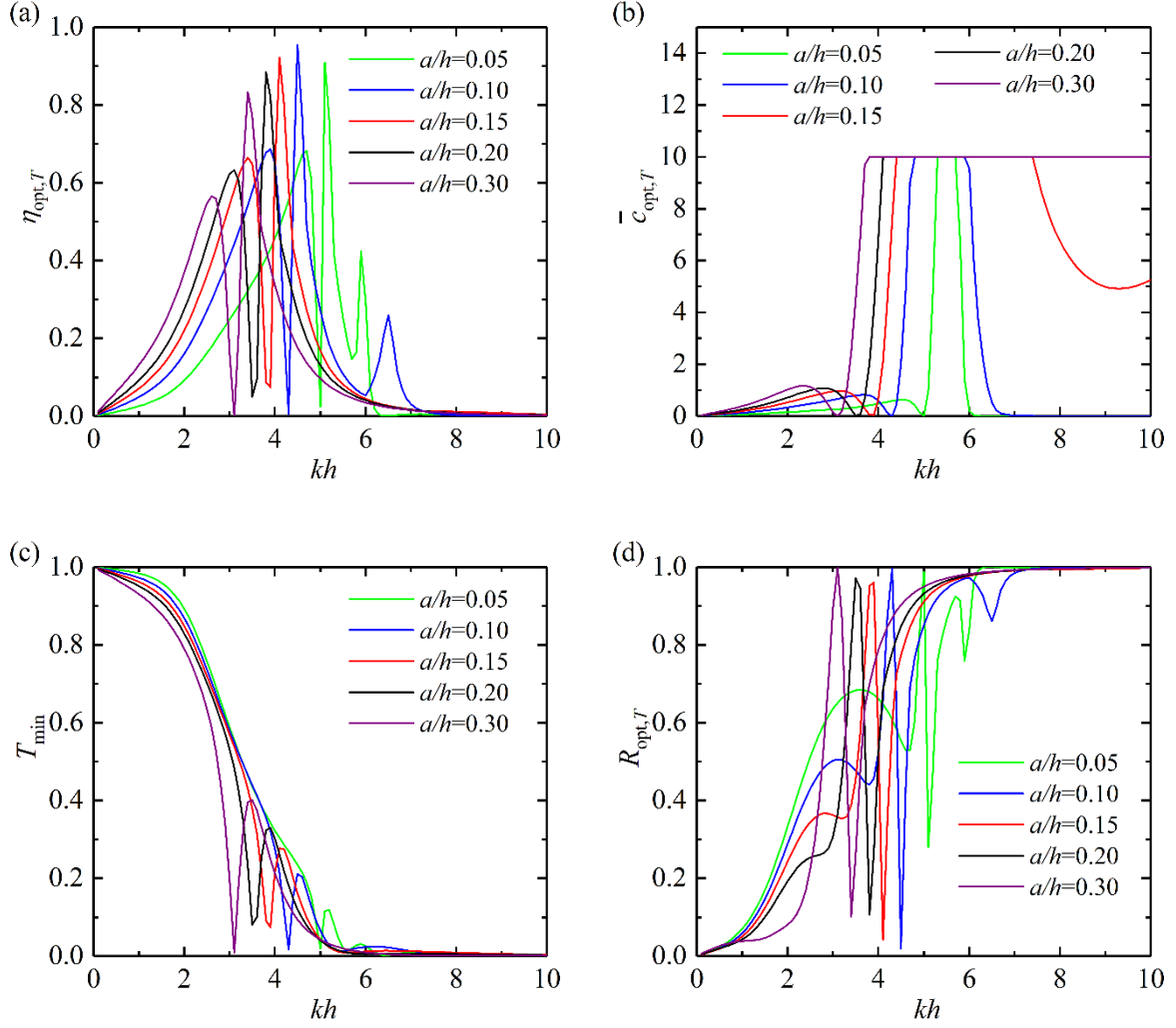


Fig.7 (a) Power extraction efficiency $\eta_{opt,T}$, (b) optimal dimensionless PTO damping $\bar{c}_{opt,T}$, (c) optimal wave transmission coefficient T_{min} and (d) wave reflection coefficient $R_{opt,T}$ versus dimensionless wave number kh for different chamber breadths a/h [$h=20$ m, $d_1/h=0.15$, $d_2/h=0.25$ and $V_0=0.1ah$].

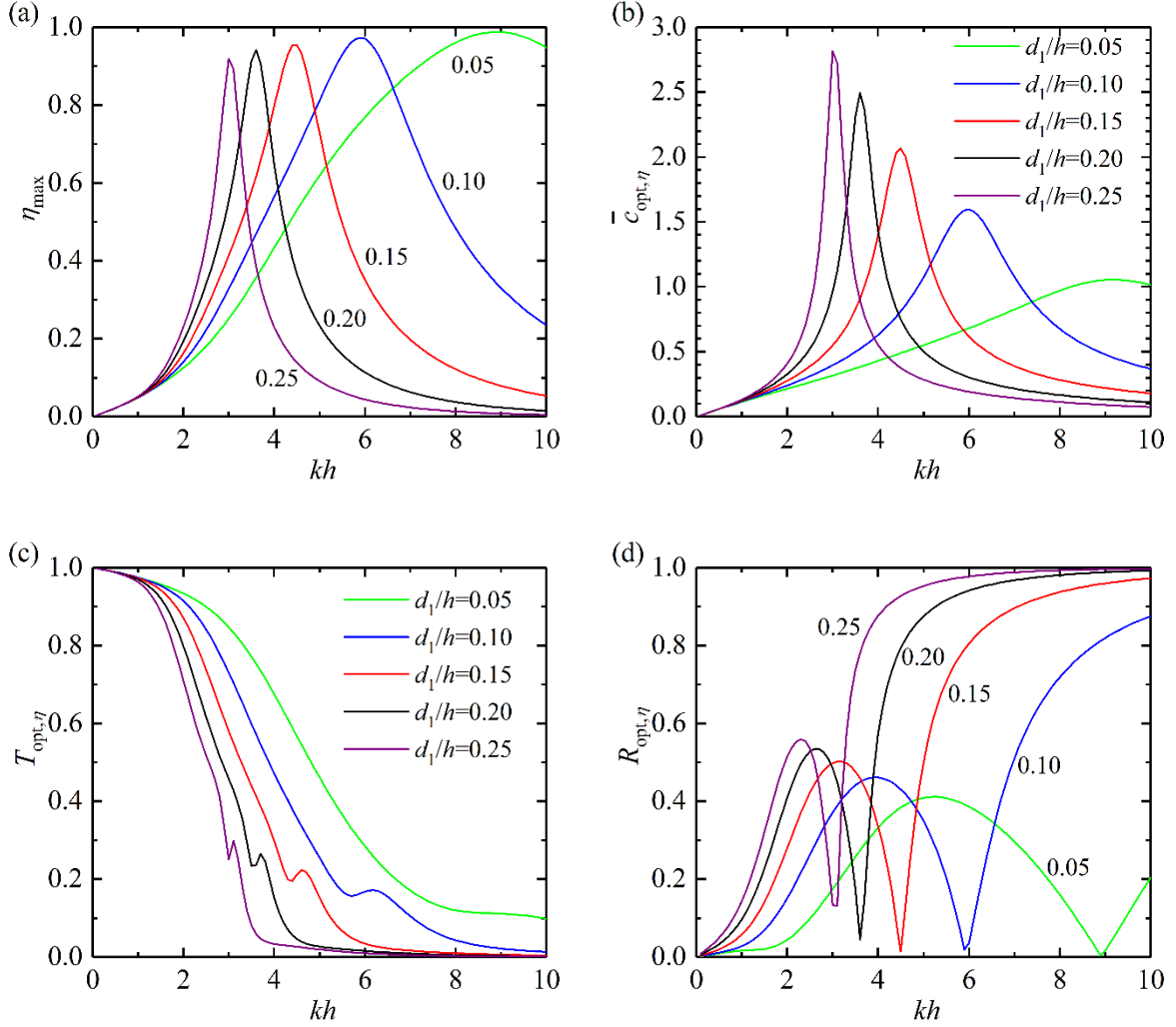
Fig. 8 illustrates the effects of wall draft when the PTO damping is optimized for maximizing the wave power extraction. The calculating parameters are: $h=20$ m, $a/h=0.1$, $d_2/h=d_1/h+0.1$, $V_0=0.1ah$, $d_1/h=0.05, 0.1, 0.15, 0.2$ and 0.25 . The variations in optimal power extraction efficiency η_{max} , optimal dimensionless PTO damping $\bar{c}_{opt,\eta}$, wave transmission coefficient $T_{opt,\eta}$ and wave reflection coefficient $R_{opt,\eta}$ are shown versus the dimensionless wave number kh . We can see from Fig. 8(a) that the peaks of η_{max} are 0.988, 0.973, 0.955, 0.942 and 0.919 for $d_1/h=0.05, 0.1, 0.15, 0.2$ and 0.25 , and occur at $kh=8.9, 5.9, 4.5, 3.6$ and 3.0 , respectively. In

general, the peak of η_{\max} is slightly lower for a deeper wall draft and occurs at a longer wave. The reason of unequal peaks of η_{\max} for different wall drafts is analogical to the effects of chamber breadth. A deeper draft resonates at a longer wave which can more easily pass through the back wall of the pile-supported OWC breakwater and the transmitted wave energy reduces the extracted wave power at resonance. It is also found the bandwidth of η_{\max} is broader for a shallower wall draft. Fig. 8 (b) indicates that a larger optimal PTO damping is desired for a deeper draft when resonance occurs.

Fig. 8(c) illustrates that when the PTO damping is optimized for η_{\max} , the effects of wall draft on the corresponding wave transmission are remarkable. The trends of $T_{\text{opt},\eta}$ for all wall drafts are a monotonic decrease for increasing kh . $T_{\text{opt},\eta}$ reduces to below 0.5 at $kh=2.6, 2.9, 3.3, 3.9$ and 4.9 for $d_1/h=0.25, 0.2, 0.15, 0.1$ and 0.05 , respectively. The largest difference in $T_{\text{opt},\eta}$ at each kh can be up to 0.694 between the deepest draft ($d_1/h=0.25$) and the shallowest draft ($d_1/h=0.05$) over all wave frequencies tested in this study. For each draft, there exists a local valley of $T_{\text{opt},\eta}$ at kh slightly smaller than resonance and a local peak of $T_{\text{opt},\eta}$ at kh slightly larger than resonance, and again this local impact to the approximately monotonic decreasing $T_{\text{opt},\eta}$ can be seen as relatively weak. As shown in Fig. 8(d), with increasing kh , $R_{\text{opt},\eta}$ firstly increases to a turning point, then decreases to a local minimum at kh where resonance occurs, and after that $R_{\text{opt},\eta}$ increases monotonically. A deeper draft generally reflects more wave energy, except for kh values around resonance.

Fig. 9 illustrates the effects of wall draft when the PTO damping is optimized for minimizing the wave transmission. The variations of power extraction efficiency $\eta_{\text{opt},T}$, optimal dimensionless PTO damping $\bar{c}_{\text{opt},T}$, optimal wave transmission coefficient T_{\min} and wave reflection coefficient $R_{\text{opt},T}$ are shown versus the dimensionless wave number kh . Comparing Fig. 9(a) with Fig. 8(a), there is at least one local valley of $\eta_{\text{opt},T}$ in the computed range of kh , which greatly harms the wave power extraction around. The valleys shift towards lower frequencies with the increase in d_1/h . We can see from Fig. 9(b) that the $\bar{c}_{\text{opt},T}$ corresponding to the first valley of $\eta_{\text{opt},T}$ is nearly zero. With increasing kh , $\bar{c}_{\text{opt},T}$ of a deeper draft reaches the nearly-zero value and the set upper

1 limit c_{ul} more rapidly but keeps at c_{ul} over a narrower range of wave frequencies. After that, $c_{opt,T}$ sharply drops
 2 to zero again and keeps at zero.



3

4

5 Fig.8 (a) Optimal power extraction efficiency η_{max} , (b) optimal dimensionless PTO damping $\bar{c}_{opt,\eta}$, (c) wave
 6 transmission coefficient $T_{opt,\eta}$ and (d) wave reflection coefficient $R_{opt,\eta}$ versus dimensionless wave number kh
 7 for different wall drafts d_1/h [$h=20m$, $a/h=0.1$, $d_2/h=d_1/h+0.1$ and $V_0=0.1ah$].

8 Comparing Fig. 9(c) with Fig. 8(c), there still exists a local valley and a local peak of wave transmission for
 9 each wall draft. The local valley of T_{min} is lower than the local valley of $T_{opt,\eta}$ for the same wall draft, and the
 10 local peaks of T_{min} and $T_{opt,\eta}$ are comparable. From around kh where the local valley occurs, T_{min} is a little
 11 lower than $T_{opt,\eta}$ over a certain range of kh , and this range is broader for a shallower draft. In contrast, for kh
 12 lower than that where the local valley occurs, T_{min} is almost the same as $T_{opt,\eta}$. Fig. 9(d) shows that $c_{opt,T}$ results

in the pile-supported OWC breakwater functioning as a reflective structure rather than as an absorbing system. Indeed, $c_{opt,T}$ contributes mainly to enhancing wave reflection, rather than to improving the power extraction. For all wall drafts, $c_{opt,T}$ hardly improves the performance in terms of protection against wave action, but does diminish the wave power extraction.

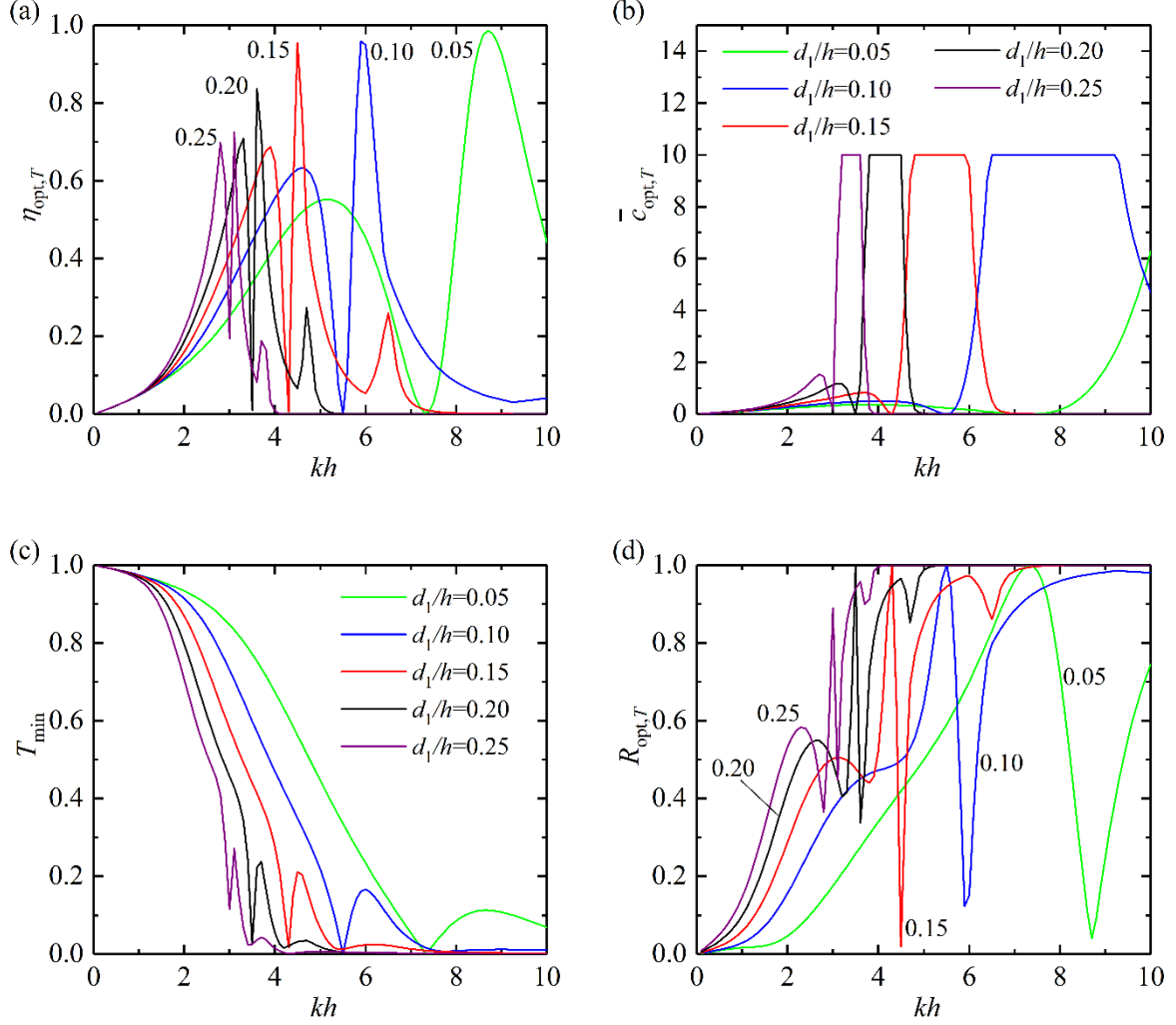


Fig.9 (a) Power extraction efficiency $\eta_{opt,T}$, (b) optimal dimensionless PTO damping $\bar{c}_{opt,T}$, (c) optimal wave transmission coefficient T_{min} and (d) wave reflection coefficient $R_{opt,T}$ versus dimensionless wave number kh for different wall drafts d_1/h [$h=20$ m, $a/h=0.1$, $d_2/h=d_1/h+0.1$ and $V_0=0.1ah$].

To sum up, optimizing the PTO damping as $c_{opt,\eta}$ to maximize the wave power extraction allows $c_{opt,\eta}$ to match the radiation damping at each wave frequency. Instead, optimizing the PTO damping as $c_{opt,T}$ to minimize the wave transmission causes $c_{opt,T}$ to lose this matching relationship with the radiation damping. Compared with

$c_{\text{opt},\eta}$, $c_{\text{opt},T}$ improve the protection performances against wave action to a very limited extent, but diminishes wave power extraction notably. The optimization to maximize power production generally improves coastal protection as well, given that the more energy that is absorbed by the structure, the less energy that is transmitted. For a pile-supported OWC breakwater, therefore, it is likely that by optimizing the PTO damping towards minimum wave transmission, the loss (in terms of power extraction) far outweighs the gain (in terms of wave protection). For this reason, only the results with the optimal PTO damping $c_{\text{opt},\eta}$ will be reported in the following.

3.4 Air chamber volume

When the air chamber volume is large enough, air compressibility becomes an important factor determining the wave power extraction and can no longer be ignored. It has been concluded that the bandwidth of high extraction efficiency with an appropriate volume can be broadened by considering the effect of air compressibility [43]. The effects of air chamber volume of pile-supported OWC breakwater on the wave power extraction and the protection against wave action are examined in this subsection.

The variations of optimal power extraction efficiency η_{max} , optimal dimensionless PTO damping $\bar{c}_{\text{opt},\eta}$, wave transmission coefficient $T_{\text{opt},\eta}$ and wave reflection coefficient $R_{\text{opt},\eta}$ versus dimensionless wave number kh are shown in Fig. 10. The calculation parameters are: $h=20$ m, $a/h=0.1$, $d_1/h=0.15$, $d_2/h=0.25$, $V_0=0, 0.5ah, 1.5ah, 3ah$ and $5ah$. The degree of air compressibility increases with V_0 , and $V_0=0$ means the air is incompressible. We can see from Fig. 10(a) that two peaks of η_{max} appear for $V_0=0.5ah$ and $1.5ah$. The presence of these two peaks, reported by Sarmento and Falcão [42] and Martins-Rivas and Mei [43], is attributed to the counteraction of radiation susceptance and air compressibility, i.e. $\mu + \mu_{\text{PTO}}=0$. Recall that $\bar{\mu}_0$ is defined as $-\mu_{\text{PTO}}\rho\sqrt{g/h}$ and $\bar{\mu}$ is defined as $\mu\rho\sqrt{g/h}$. Fig. 11 shows the variations of $\bar{\mu}_0$ for different air chamber volumes V_0 and $\bar{\mu}$ versus dimensionless wave number kh . As V_0 increases, the $\bar{\mu}_0$ curves are getting more and more downwardly oblique. There exists two interaction points between $\bar{\mu}_0$ curve and $\bar{\mu}$ curve for $V_0=0.5ah$ and $1.5ah$, corresponding to the presences of two peaks of η_{max} . When V_0 exceeds a certain value, e.g., $V_0=5ah$, $\bar{\mu}_0$ curve begins to have no interaction with $\bar{\mu}$ curve. Correspondingly, the peak η_{max} for $V_0=5ah$ is lower than

other air chamber volumes. In addition, Fig. 10 (b) indicated that a larger optimal PTO damping is desired for a larger air chamber volume when resonance occurs.

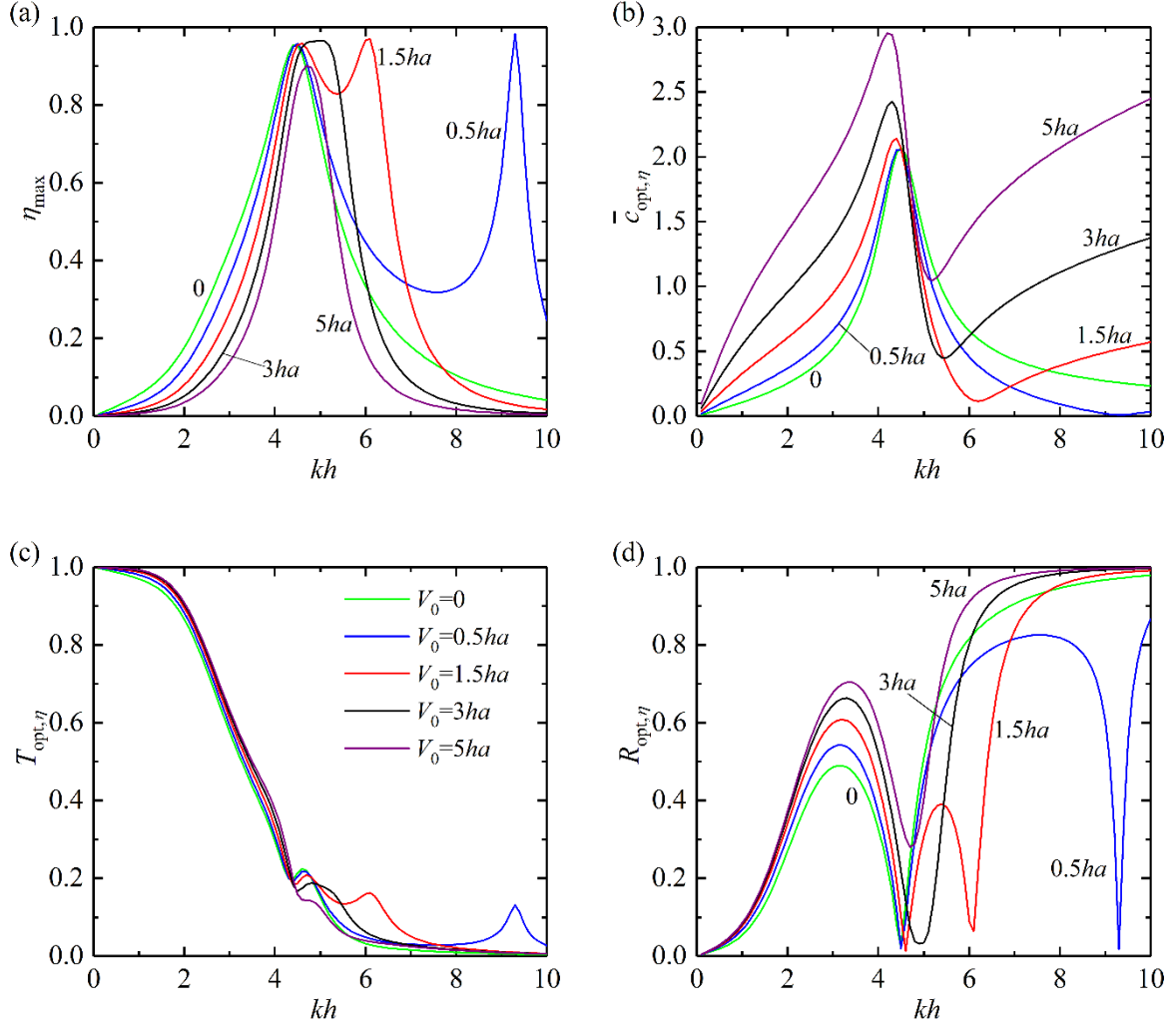


Fig.10 (a) Optimal power extraction efficiency η_{\max} , (b) optimal dimensionless PTO damping $\bar{c}_{\text{opt},\eta}$, (c) wave transmission coefficient $T_{\text{opt},\eta}$ and (d) wave reflection coefficient $R_{\text{opt},\eta}$ versus dimensionless wave number kh for different air chamber volumes V_0 [$h=20$ m, $a/h=0.1$, $d_1/h=0.15$ and $d_2/h=0.25$].

As shown in Fig. 10(c), wave transmission for different air chamber volumes is not fundamentally different. It is interesting to note that around the values of kh where peaks of η_{\max} occur, there are corresponding local peaks of $T_{\text{opt},\eta}$, albeit not very marked. It may be inferred that the resonances increase somewhat the wave energy passing through the back-wall of the pile-supported OWC breakwater. For $V_0=0.5ah$ and $1.5ah$, which correspond to two

peaks of η_{\max} , there exists a second local peak for $T_{\text{opt},\eta}$, but it is a little lower than the first local peak and happens for shorter waves. It can be concluded that air compressibility increases the transmission coefficient for certain particular wave conditions, but at an insignificant level.

In brief, for a pile-supported OWC breakwater, the effect of air compressibility can counteract the radiation susceptance more than once in the computed range of wave conditions with appropriate air chamber volumes. The multiple counteractions can enhance the bandwidth of high extraction efficiency by the appearance of multi-peak of η_{\max} , but are detrimental to the protection against wave action fortunately at an insignificant level. For multiple counteractions to occur, the air chamber volume should be large enough. As illustrated in Fig. 11, at least $V_0 = 0.5ah$ is required in this case. It means that the freeboard height of the air chamber must be $0.5h$, i.e., half of the water depth, which is too large from the standpoint of engineering practice. For a more reasonable value, e.g., $V_0 = 0.1ah$, the air compressibility may be ignored.

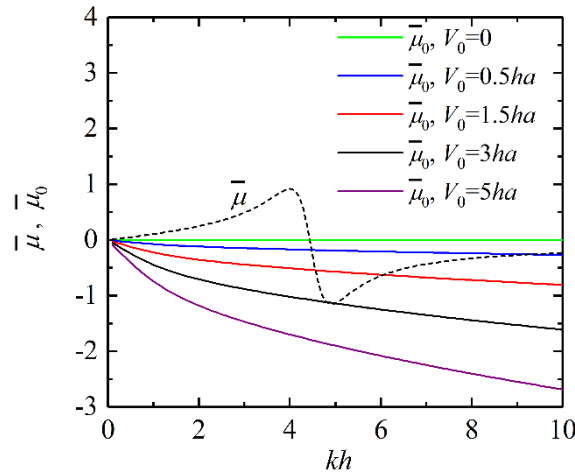


Fig. 11 $\bar{\mu}_0$ coefficient of different air chamber volumes V_0 and dimensionless radiation susceptance $\bar{\mu}$ versus dimensionless wave number kh [$h=20$ m, $a/h=0.1$, $d_1/h=0.15$ and $d_2/h=0.25$].

3.5 Practical optimization strategy

Hereinbefore, the optimization of PTO damping for maximizing wave power extraction over all wave frequencies was ideal, in the sense that the characteristics of the turbine system, e.g., the blade angles or rotational speed, were assumed to be adjusted in real time according to the incoming wave spectrum. This ideal optimization is hard to achieve in practice. A more practical optimization strategy, proposed by Lovas et al. [46], considered only a

discrete series of values for the PTO damping, each value corresponding to a certain frequency band. In the following, this strategy is adopted, and the resulting wave power extraction and protection against wave action are examined.

As an example, the calculation parameters are: $h=20$ m, $a/h=0.1$, $d_1/h=0.15$, $d_2/h=0.25$ and $V_0=0.1ha$. The variations of dimensionless PTO damping \bar{c}_{PTO} , power extraction efficiency η and wave transmission coefficient T from the ideal optimization strategy are shown in Fig. 12 as solid black lines for comparison. As shown in Fig. 12(a), two values of dimensionless PTO damping are taken as $\bar{c}_1=2.067$ being the $\bar{c}_{\text{opt},\eta}$ for peak of η_{max} and $\bar{c}_2=0.550$ being the arithmetic mean of $\bar{c}_{\text{opt},\eta}$ over $0 \leq kh \leq 10$. The corresponding power extraction efficiency η and wave transmission coefficient T for \bar{c}_1 and \bar{c}_2 are shown in Figs. 12(b) and 12(c) as blue and red symbols, respectively. We can see from Fig. 12(b), η for \bar{c}_1 is almost identical with η_{max} over a certain range of kh around where the peak η_{max} occurs, and η for \bar{c}_2 is very close to η_{max} over other kh . Two intersection points between the curves of η for \bar{c}_1 and η for \bar{c}_2 occur at $kh=3.8$ and $kh=5.2$. For the practical optimization strategy, the dimensionless PTO damping \bar{c}_{PTO} piecewise constants are: $\bar{c}_1=2.067$ for $3.8 \leq kh \leq 5.2$ and $\bar{c}_2=0.550$ for $kh \leq 3.8$ and $kh \geq 5.2$, as replotted in Fig. 13(a). The corresponding power extraction efficiency η and wave transmission coefficient T with the practical optimization strategy are shown in Figs. 13(b) and 13(c). It is found that it is possible to obtain a power extraction efficiency close to η_{max} and a wave transmission coefficient close to $T_{\text{opt},\eta}$ with only two values of PTO damping. Indeed, with two values the largest difference between the ideal and practical optimization strategies is only 0.08 in terms of power extraction efficiency (difference between η_{max} and η) and a mere 0.03 in terms of wave transmission (difference between $T_{\text{opt},\eta}$ and T). Although these differences can be further diminished by setting more piecewise constants for \bar{c}_{PTO} , the two-level optimization strategy has been proven to be efficient enough over all wave frequencies. The fewer levels of \bar{c}_{PTO} , the easier it is to implement the strategy in practice. With the two-level optimization strategy, both the wave power extraction and the protection against wave action can be guaranteed for the pile-supported OWC breakwater.

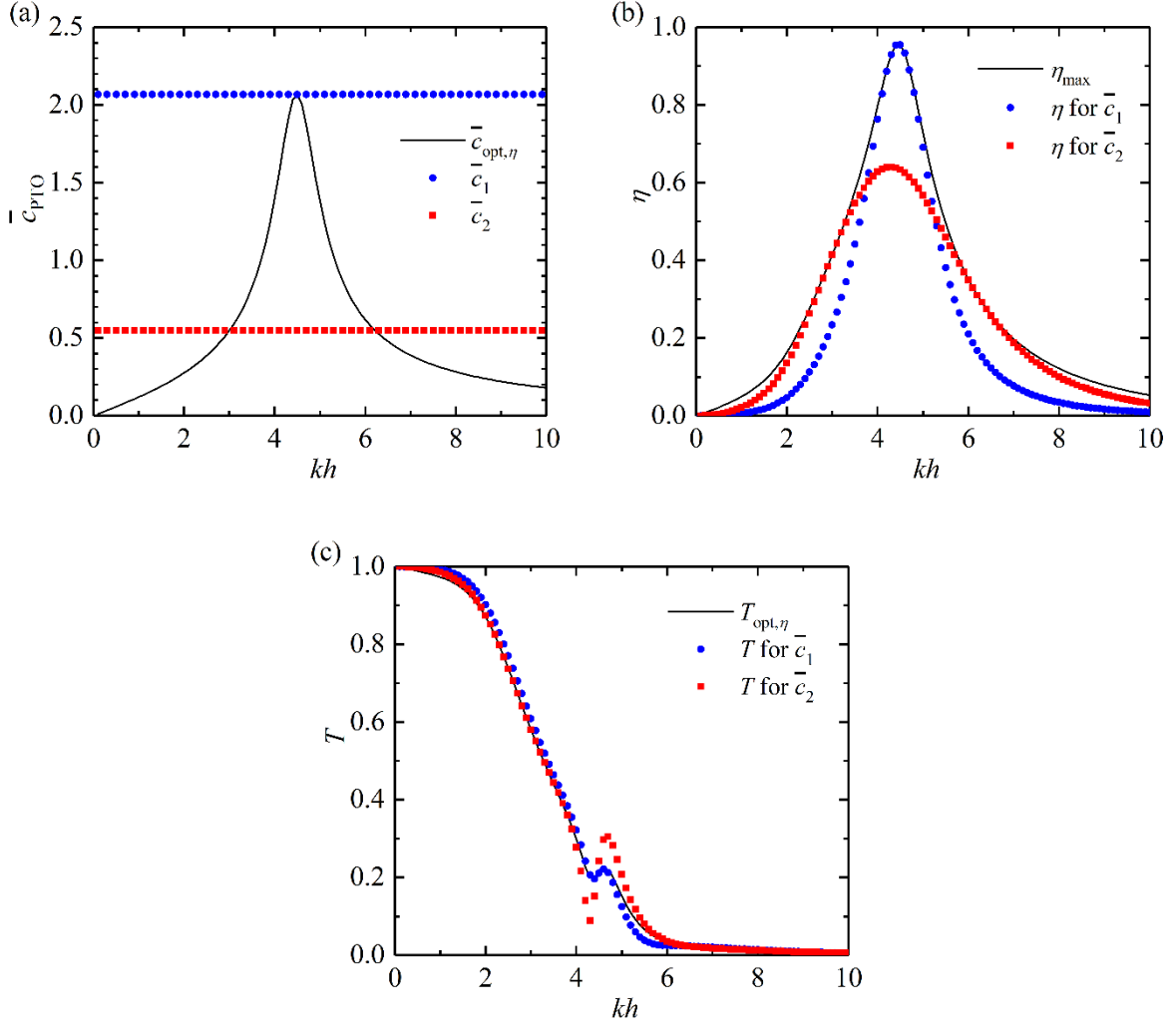


Fig.12 (a) Dimensionless PTO damping \bar{c}_{PTO} , (b) power extraction efficiency η and (c) wave transmission coefficient T versus dimensionless wave number kh from ideal optimization of PTO damping and two values of PTO damping [$h=20$ m, $a/h=0.1$, $d_1/h=0.15$, $d_2/h=0.25$ and $V_0=0.1ah$].

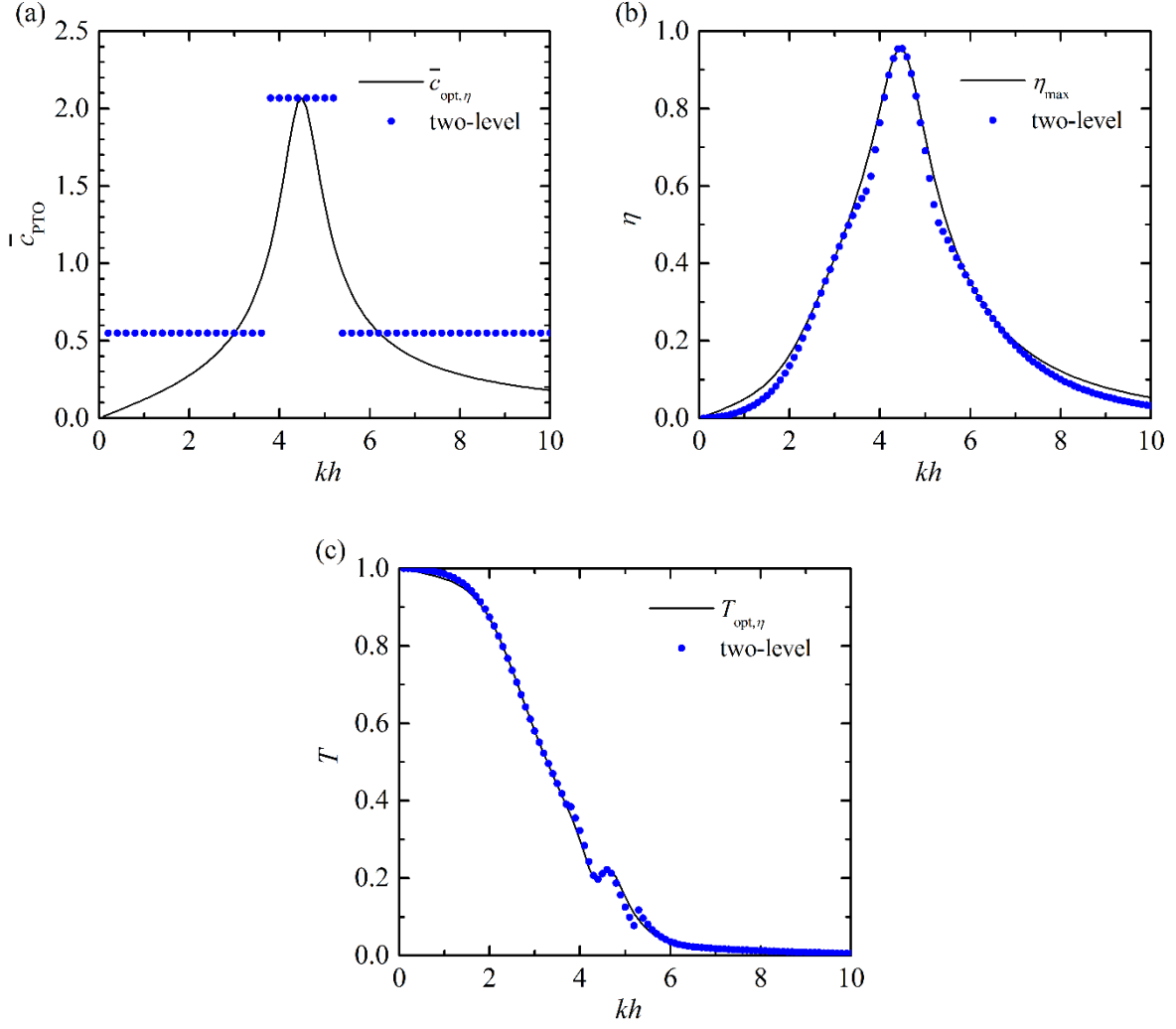


Fig.13 Optimization of (a) dimensionless PTO damping \bar{c}_{PTO} , (b) power extraction efficiency η and (c) wave transmission coefficient T from ideal strategy and practical two-level strategy [$h=20$ m, $a/h=0.1$, $d_1/h=0.15$, $d_2/h=0.25$ and $V_0=0.1ah$].

4. Conclusions

The hydrodynamic performance of a pile-supported OWC breakwater was modeled analytically based on linear wave theory and the method of matched eigenfunction expansion. A local increase in the back-wall draft, proposed as an economical means to enhance performance, was shown to effectively increase wave power extraction and decrease wave transmission. Initially, the PTO damping was optimized ideally, targeting two objectives: maximum power extraction and minimum wave transmission. The effects of chamber breadth, wall draft and air chamber volume were examined. Given the difficulties for the practical implementation of the ideal optimization strategy, a

more practical strategy to optimize PTO damping was explored too, with the same objectives. The following conclusions can be drawn from this study.

First, an optimization towards maximum power extraction can also lead to satisfactory wave transmission, but an optimization towards minimum wave transmission results in a significant reduction in wave power extraction. For this reason, optimizing the PTO damping towards maximum power extraction is preferable.

Second, as regards the effects of the chamber breadth, a wider chamber can enhance the extraction bandwidth for longer waves, albeit at the expense of a slightly lower peak value; wave transmission and, therefore, protection against wave action was found to be little sensitive to chamber breadth. As for the wall draft, a shallower wall can enhance the power extraction bandwidth for shorter waves, but at the expense of greater wave transmission. This sets a limit to the minimum draft that is required for practical applications.

Third, the air compressibility effect can enhance the bandwidth of high extraction efficiency with appropriate air chamber volumes, but can also increase slightly the transmission coefficient for certain particular wave conditions. In any case, it is found that, at engineering scales, the air chamber volume is too small for the air compressibility effect to play a significant role in the performance of the pile-supported OWC breakwater.

Finally, applying the two-level optimization strategy, both the wave power extraction and the protection against wave action can be as efficient as the ideal optimization of PTO damping, with the advantage of being easier to implement in practice.

In summary, the pile-supported OWC breakwater, with the dual function of generating carbon-free energy and providing shelter against wave action, was shown to be a promising multifunction marine structure with the potential to protect maritime activities in deeper water than conventional breakwaters (e.g., far away from the mainland) and provide electricity efficiently for the same, or other, activities. Future work will consider the effect of non-linear PTO system, e.g., a radial or bi-radial turbine, in the time-domain as well as the performance in irregular wave conditions, which may lead to more realistic results.

Acknowledgments

This work was supported by the National Natural Science Foundation of China (No. 51609211), Natural Science Foundation of Zhejiang Province (No. LY19E090007), Zhoushan-ZJU Joint Project (No. 2017C82226), Intelligent Community Energy (ICE), INTERREG V FCE, and European Commission (No. 5025).

Appendix

After inserting the expression of the air pressure fluctuation inside the chamber p into Eq. (49), we have

$$T = \left| 1 + \frac{i\omega}{gA} Z_0(0) \left(A_{b,0}^{(1)} + \frac{Q_e}{c_{\text{PTO}} + c + i(\mu + \mu_{\text{PTO}})} A_{b,0}^{(2)} \right) \right|, \quad (\text{A1})$$

from which it can be inferred that for an absolute value of the PTO damping coefficient tending to infinity ($c_{\text{PTO}} \rightarrow \pm\infty$), the wave transmission coefficient will tend to

$$T_0 = \left| 1 + \frac{i\omega}{gA} Z_0(0) A_{b,0}^{(1)} \right|. \quad (\text{A2})$$

Fig. A1 presents an example which illustrates the effect of PTO damping on the wave transmission. Here the calculating parameters are: $h=20$ m, $a/h=0.1$, $d_1/h=0.15$, $d_2/h=0.25$, $V_0=0.1ah$ and $kh=4.0$. With increasing \bar{c}_{PTO} , the wave transmission coefficient T firstly increases from just above T_0 to the peak value, later sharply drops to the valley value in a relatively narrow range of \bar{c}_{PTO} , and finally increases to just below T_0 . Actually, for any certain wave condition tested in this study, the variation of T versus \bar{c}_{PTO} is a curve shaped like the letter “N” and intersect with T_0 at \bar{c}_{PTO} around zero.

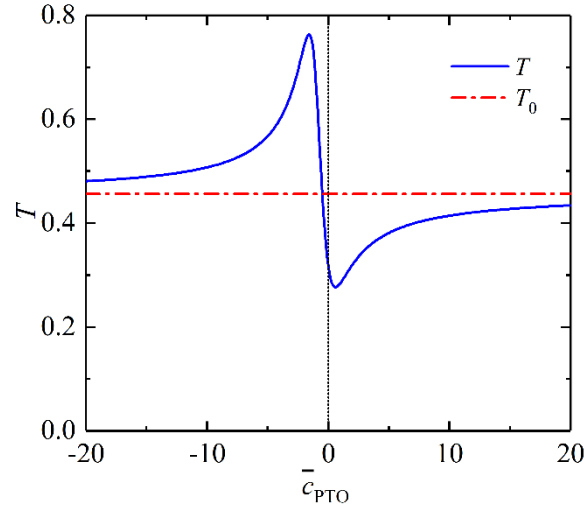


Fig. A1 Wave transmission coefficient T versus dimensionless PTO damping \bar{c}_{PTO} [$h=20$ m, $a/h=0.1$, $d_1/h=0.15$, $d_2/h=0.25$, $V_0=0.1ah$ and $kh=4.0$].

The PTO damping coefficients c_1 and c_2 , corresponding to the peak and valley values of T , respectively,

can be evaluated by letting $\partial T / \partial c_{\text{PTO}} = 0$ as

$$\begin{cases} c_1 \\ c_2 \end{cases} = \begin{cases} \min \\ \max \end{cases} \left(\frac{-a_t \pm \sqrt{a_t^2 + 4b_t \left[b_t (c^2 + (\mu + \mu_{\text{PTO}})^2) - a_t c \right]}}{2b_t} \right), \quad (\text{A3})$$

where

$$a_t = \left| Q_e A_{b,0}^{(2)} \right|^2 + 2 \operatorname{Re} \left[Q_e A_{b,0}^{(2)} \left(A_{b,0}^{(1)*} + \frac{igA}{\omega Z_0(0)} \right) \left[c - i(\mu + \mu_{\text{PTO}}) \right] \right], \quad (\text{A4})$$

and

$$b_t = \operatorname{Re} \left[Q_e A_{b,0}^{(2)} \left(A_{b,0}^{(1)*} + \frac{igA}{\omega Z_0(0)} \right) \right]. \quad (\text{A5})$$

For all the cases tested in this study, both a_t and b_t are positive and meanwhile $c_1 < 0 < c_2$, therefore the optimal

PTO damping coefficient for minimizing the wave transmission is

$$c_{\text{opt},T} = \frac{-a_t + \sqrt{a_t^2 + 4b_t \left[b_t (c^2 + (\mu + \mu_{\text{PTO}})^2) - a_t c \right]}}{2b_t}. \quad (\text{A6})$$

Since in practice the value of PTO damping coefficient will not be too large, here we set an upper limit for the PTO

damping coefficient as c_{ul} , i.e., c_{PTO} is always not larger than c_{ul} . The optimal PTO damping coefficient at the

range of $[0, c_{\text{ul}}]$ for minimizing the wave transmission is

$$c_{\text{opt},T} = \min \left\{ \frac{-a_t + \sqrt{a_t^2 + 4b_t \left[b_t (c^2 + (\mu + \mu_{\text{PTO}})^2) - a_t c \right]}}{2b_t}, c_{\text{ul}} \right\}. \quad (\text{A7})$$

References

- [1] Huang Z, Li Y, Liu Y. Hydraulic performance and wave loadings of perforated/slotted coastal structures: A review. Ocean Engineering. 2011;38:1031-53.
- [2] Ji C-Y, Chen X, Cui J, Yuan Z-M, Incecik A. Experimental study of a new type of floating breakwater. Ocean Engineering. 2015;105:295-303.
- [3] Wang Y, Wang G, Li G. Experimental study on the performance of the multiple-layer breakwater. Ocean Engineering. 2006;33:1829-39.
- [4] Liu Y, Li Y. Wave interaction with a wave absorbing double curtain-wall breakwater. Ocean Engineering. 2011;38:1237-45.

- [5] Falcão AF. Wave energy utilization: A review of the technologies. *Renewable and sustainable energy reviews*. 2010;14:899-918.
- [6] He F, Huang Z. Using an oscillating water column structure to reduce wave reflection from a vertical wall. *Journal of Waterway, Port, Coastal, and Ocean Engineering*. 2016;142:04015021.
- [7] Abanades J, Flor-Blanco G, Flor G, Iglesias G. Dual wave farms for energy production and coastal protection. *Ocean & Coastal Management*. 2018;160:18-29.
- [8] Washio Y, Osawa H, Nagata Y, Fujii F, Furuyama H, Fujita T. The offshore floating type wave power device" Mighty Whale": open sea tests. *The Tenth International Offshore and Polar Engineering Conference: International Society of Offshore and Polar Engineers*; 2000.
- [9] He F, Leng J, Zhao X. An experimental investigation into the wave power extraction of a floating box-type breakwater with dual pneumatic chambers. *Applied Ocean Research*. 2017;67:21-30.
- [10] Astariz S, Iglesias G. The economics of wave energy: A review. *Renew Sust Energ Rev*. 2015;45:397-408.
- [11] Contestabile P, Lauro ED, Buccino M, Vicinanza D. Economic assessment of Overtopping Breakwater for Energy Conversion (OBREC): a case study in Western Australia. *Sustainability*. 2016;9.
- [12] Contestabile P, Ferrante V, Lauro ED, Vicinanza D. Prototype overtopping breakwater for wave energy conversion at port of Naples. *26th International Ocean and Polar Engineering Conference*. Rhodes, Greece 2016. p. 616-21.
- [13] López I, Pereiras B, Castro F, Iglesias G. Optimisation of turbine-induced damping for an OWC wave energy converter using a RANS-VOF numerical model. *Applied Energy*. 2014;127:105-14.
- [14] He F, Huang Z. Hydrodynamic performance of pile-supported OWC-type structures as breakwaters: An experimental study. *Ocean Engineering*. 2014;88:618-26.
- [15] Ning D, Zhao X, Göteman M, Kang H. Hydrodynamic performance of a pile-restrained WEC-type floating breakwater: An experimental study. *Renewable Energy*. 2016;95:531-41.
- [16] Mustapa MA, Yaakob OB, Ahmed YM, Rheem C-K, Koh KK, Adnan FA. Wave energy device and breakwater integration: A review. *Renewable and Sustainable Energy Reviews*. 2017;77:43-58.
- [17] He F, Li M, Huang ZJE. An experimental study of pile-supported OWC-type breakwaters: energy extraction and vortex-induced energy loss. *Energies*. 2016;9:540.
- [18] Margheritini L, Vicinanza D, Frigaard P. SSG wave energy converter: Design, reliability and hydraulic performance of an innovative overtopping device. *Renewable Energy*. 2009;34:1371-80.
- [19] Elhanafi A, Macfarlane G, Fleming A, Leong ZJAE. Experimental and numerical investigations on the hydrodynamic performance of a floating-moored oscillating water column wave energy converter. *Applied Energy*. 2017;205:369-90.
- [20] Zheng S, Zhang Y. Theoretical modelling of a new hybrid wave energy converter in regular waves. *Renewable Energy*. 2018;128:125-41.
- [21] Ning D, Zhou Y, Zhang C. Hydrodynamic modeling of a novel dual-chamber OWC wave energy converter. *Applied Ocean Research*. 2018;78:180-91.
- [22] Sheng W. Power performance of BBDB OWC wave energy converters. *Renewable Energy*. 2019;132:709-22.
- [23] López I, Castro A, Iglesias G. Hydrodynamic performance of an oscillating water column wave energy converter by means of particle imaging velocimetry. *Energy*. 2015;83:89-103.
- [24] Elhanafi A, Fleming A, Macfarlane G, Leong ZJE. Numerical energy balance analysis for an onshore oscillating water column-wave energy converter. *Energy*. 2016;116:539-57.
- [25] He F, Huang Z. Characteristics of orifices for modeling nonlinear power take-off in wave-flume tests of oscillating water column devices. *Journal of Zhejiang University-SCIENCE A*. 2017;18:329-45.
- [26] Wang R-q, Ning D-z, Zhang C-w, Zou Q-p, Liu Z. Nonlinear and viscous effects on the hydrodynamic performance of a fixed OWC wave energy converter. *Coastal Engineering*. 2018;131:42-50.

- [27] Wu B, Chen T, Jiang J, Li G, Zhang Y, Ye Y. Economic assessment of wave power boat based on the performance of “Mighty Whale” and BBDB. *Renewable and Sustainable Energy Reviews*. 2018;81:946-53.
- [28] He F, Huang Z, Wing-Keung Law A. Hydrodynamic performance of a rectangular floating breakwater with and without pneumatic chambers: An experimental study. *Ocean Engineering*. 2012;51:16-27.
- [29] Falcão AF, Henriques JC. Oscillating-water-column wave energy converters and air turbines: A review. *Renewable Energy*. 2016;85:1391-424.
- [30] Boccotti P. Caisson breakwaters embodying an OWC with a small opening- Part I: Theory. *Ocean Eng*. 2007;34:806-19.
- [31] Ojima R, Suzumura S, Goda Y. Theory and experiments on extractable wave power by an oscillating water-column type breakwater caisson. *Coastal Engineering Journal*. 1984;27:315-26.
- [32] Takahashi S, Nakada H, Ohneda H, Shikamori M. Wave power conversion by a prototype wave power extracting caisson in Sakata Port. *Proceedings of the 23rd international conference on coastal engineering*1992. p. 3440-53.
- [33] Raju V, Jayakumar J, Neelamani S. Concrete Caisson For Also Kw Wave Energy Pilot Plant: Design, Construction And Installation Aspects. *The Second International Offshore and Polar Engineering Conference: International Society of Offshore and Polar Engineers*; 1992. p. 584-91.
- [34] Torre-Enciso Y, Ortubia I, de Aguilera LL, Marqués J. Mutriku wave power plant: from the thinking out to the reality. *Proceedings of the 8th European Wave and Tidal Energy Conference, Uppsala, Sweden*2009. p. 319-29.
- [35] Arena F, Romolo A, Malara G, Ascanelli A. On design and building of a U-OWC wave energy converter in the Mediterranean Sea: a case study. *ASME 2013 32nd International Conference on Ocean, Offshore and Arctic Engineering: American Society of Mechanical Engineers*; 2013. p. 11593.
- [36] Arena F, Romolo A, Malara G, Fiamma V, Laface V. The first full operative U-OWC plants in the port of Civitavecchia. *ASME 2017 36th International Conference on Ocean, Offshore and Arctic Engineering*. Trondheim, Norway2017. p. 11.
- [37] Viviano A, Naty S, Foti E, Bruce T, Allsop W, Vicinanza D. Large-scale experiments on the behavior of a generalized Oscillating Water Column under random waves. *Renew Energ*. 2016;99:875-87.
- [38] Pawitan KA, Dimakopoulos AS, Vicinanza D, Allsop W, Bruce T. A loading model for an OWC caisson based upon large-scale measurements. *Coast Eng*. 2019;145:1-20.
- [39] He F, Huang Z, Law AW-K. An experimental study of a floating breakwater with asymmetric pneumatic chambers for wave energy extraction. *Applied energy*. 2013;106:222-31.
- [40] Evans D. The oscillating water column wave-energy device. *IMA Journal of Applied Mathematics*. 1978;22:423-33.
- [41] Evans D. Wave-power absorption by systems of oscillating surface pressure distributions. *Journal of Fluid Mechanics*. 1982;114:481-99.
- [42] Sarmento A, Falcão AFdO. Wave generation by an oscillating surface-pressure and its application in wave-energy extraction. *Journal of Fluid Mechanics*. 1985;150:467-85.
- [43] Martins-Rivas H, Mei CC. Wave power extraction from an oscillating water column at the tip of a breakwater. *Journal of Fluid Mechanics*. 2009;626:395-414.
- [44] Sarmento AJNA. Wave flume experiments on two-dimensional oscillating water column wave energy devices. *Experiments in Fluids*. 1992;12:286-92.
- [45] Evans DV, Porter R. Hydrodynamic characteristics of an oscillating water column device. *Appl Ocean Res*. 1995;17:155-64.
- [46] Lovas S, Mei CC, Liu Y. Oscillating water column at a coastal corner for wave power extraction. *Applied Ocean Research*. 2010;32:267-83.
- [47] Elhanafi A, Fleming A, Macfarlane G, Leong Z. Underwater geometrical impact on the hydrodynamic performance of an offshore oscillating water column–wave energy converter. *Renewable Energy*. 2017;105:209-31.

- 1 [48] Zheng S, Zhang Y. Wave diffraction and radiation by multiple rectangular floaters. J Hydraul Res. 2016;54:102-15.
- 2 [49] Falnes J. Ocean waves and oscillating systems: linear interactions including wave-energy extraction: Cambridge
- 3 university press; 2002.
- 4 [50] Falnes J, McIver P. Surface wave interactions with systems of oscillating bodies and pressure distributions. Applied
- 5 Ocean Research. 1985;7:225-34.

6